JGR Solid Earth

RESEARCH ARTICLE
10.1029/2021JB022039

Weakening Mechanisms in a Basalt-Hosted Subduction Megathrust Fault Segment, Southern Alaska

Zoe Braden[1] **and Whitney M. Behr**[1]

[1]Department of Earth Sciences, Structural Geology and Tectonics Group, Geological Institute, ETH Zurich, Zurich, Switzerland

Key Points:

- Seafloor alteration produces hydrous phases and phyllosilicates that impact P_f and frictional strength of basalt
- Basalt weakens through a consistent pattern of deformation during subduction that depends on P_f and phyllosilicate content
- Subducted basalt hosts larger shear stresses than sediment megathrusts and deforms at a narrower width, suggesting faster strain rates

Supporting Information:

Supporting Information may be found in the online version of this article.

Correspondence to:

Z. Braden,
zoe.braden@erdw.ethz.ch

Citation:

Braden, Z., & Behr, W. M. (2021). Weakening mechanisms in a basalt-hosted subduction megathrust fault segment, southern Alaska. *Journal of Geophysical Research: Solid Earth*, *126*, e2021JB022039. https://doi.org/10.1029/2021JB022039

Received 10 MAR 2021
Accepted 26 AUG 2021

Abstract Basaltic and gabbroic rocks that define the seafloor have been suggested to act as sources of rheological heterogeneity during subduction, with the capacity to enhance or dampen seismicity. Despite this, relatively little is known from the rock record regarding the progression and conditions of mafic oceanic crust deformation during subduction, particularly in the shallow megathrust region of the seismogenic zone. We describe subduction-related deformation structures and characterize deformation conditions from an exhumed, basalt-hosted megathrust in the Chugach accretionary complex of south-central Alaska. Rocks in the Chugach preserve a record of seafloor mineralogical changes from pre-subduction, hydrothermal circulation that produced sheet silicates with a lower frictional strength than intact basalt. Pre-subduction alteration also served to introduce hydrous phases that can expel water during deformation and raise the pore fluid pressure. Once strain localized within basalts onto a megathrust fault plane at lithostatic pore fluid pressures, the basalt weakened further through a combination of cataclasis, dilatational shear fracturing, and slip on chlorite-rich shear bands. This process occurred in a narrower fault zone, and at higher maximum differential stress and greater pore fluid pressure fluctuations than recorded in some sediment-hosted megathrusts at similar pressure and temperature conditions. Our data indicate that when the lower plate contains basalt bathymetric features, basalt dismembers during subduction into a chlorite-rich fault gouge that surrounds lenses or slices of intact, less-altered basalt.

Plain Language Summary When one tectonic plate slides beneath another (the process of subduction), the surface roughness and the composition of the lower plate can change how easily and how rapidly this convergence occurs. Typically, the subduction process is neither smooth nor steady, and this results in seismic activity that varies in magnitude—small to large—and character—from fast, infrequent earthquakes to slow and frequently recurring earthquakes. It is critical to determine the properties of the rocks that make up the lower plate, so that we can better understand which features lead to various types of earthquake activity. We describe the characteristics of volcanic rocks that once occupied the lower plate and that are now exposed in south-central Alaska. These rocks record a pattern of breakdown that is dependent on compositional changes from chemical alteration on the seafloor prior to subduction and high fluid pressures during subduction. Our data indicate that volcanic topographic features on the seafloor do break apart and undergo significant compositional and mechanical changes, and the strength of the resulting rock is controlled primarily by the strength of the mineral chlorite.

1. Introduction

The shallow plate interface in subduction zones accommodates both slow slip events and megathrust earthquakes as a function of pressure-temperature conditions, compositional and fluid-pressure heterogeneities, and deformation mechanisms. On the subduction interface, the primary materials present (e.g., pelagic and terrigenous sediments and mafic volcanic rocks) are interpreted to exhibit different rheological properties that may be the source of diverse mechanical and seismic behavior (e.g., Barnes et al., 2020; Ikari et al., 2020; Saffer & Wallace, 2015). Basaltic crust associated with subducting seamounts and/or other topographic features on the seafloor, for example, is hypothesized to produce "roughness" or asperities that affect megathrust earthquake nucleation and rupture migration patterns (Cloos, 1992; Scholz & Small, 1997; Tréhu et al., 2012; Watts et al., 2010). In particular, these bathymetric features have been suggested to cause strong plate coupling and either generate or promote megathrust earthquakes (Bilek et al., 2003; Cloos, 1992; Husen et al., 2002; Wang & Bilek, 2014). Alternatively, basalt slabs or seamounts may form zones of weaker

plate coupling through the generation of off-fault deformation or fracture networks that act as barriers to rupture propagation (e.g., Kodaira et al., 2000; Lallemand et al., 2018; Mochizuki et al., 2008; Van Rijsingen et al., 2018; Wang & Bilek, 2014).

In addition to the potential role of lithological heterogeneity in influencing subduction megathrust seismicity through the generation of frictional asperities, heterogeneous mixing of different rock types may be essential for slow slip and tremor events on both the shallow and deep interface (Barnes et al., 2020; Beall et al., 2019; Behr & Bürgmann, 2021; Fagereng et al., 2014; Fagereng & Sibson, 2010; Kirkpatrick et al., 2021; Kotowski & Behr, 2019). Tectonic melanges, in which blocks of basalt are embedded in a sedimentary matrix, are common features at these margins, and slip along the boundaries of basalt blocks on the interface has also been suggested to generate slow slip-type phenomena (Phillips, Motohashi, Ujiie, & Rowe, 2020). At deeper subduction depths, metabasalt or eclogite blocks have been shown to act as brittle blocks within a viscous matrix (Behr et al., 2018). Understanding the evolution of basalt mechanical properties with increasing strain and at different pressure-temperature conditions may thus be an essential aspect of understanding the styles of transient slip, and earthquake nucleation and recurrence.

Over million-year timescales, sediment-starved, basalt-dominated subduction interfaces have also been suggested to affect several important aspects of larger-scale subduction dynamics, including interplate mechanical coupling and the development of upper plate orogenic topography (e.g., Lamb & Davis, 2003; Sobolev & Babeyko, 2005), long-term subduction erosion (e.g., Von Huene et al., 2004), and subduction plate velocities (Behr & Becker, 2018). This is because sediment-rich subduction environments are anticipated to host frictionally weaker materials and/or generate more fluid overpressure, thus reducing the effective normal stress and shear strength of faults compared to their basalt-dominated counterparts (Fagereng et al., 2014; Fagereng & Sibson, 2010; Kimura et al., 2012; Li et al., 2018; Saffer & Bekins, 2006; Saffer & Marone, 2003; Saffer & Wallace, 2015; Zhang et al., 2017). In contrast, thin sediment cover and the resulting heterogeneous plate interface may affect slab geometry and size, and development of the accretionary wedge, forearc topography, and along-strike segmentation of plate-coupled regions (e.g., Cosentino et al., 2018; Li et al., 2018; Malatesta et al., 2013). If basaltic rocks maintain their relative "strength" on the interface over long timescales compared to subducted sedimentary rocks, fundamental differences in orogenic development and slab-mantle interactions are anticipated.

The hypothesis that basalt-dominated subduction environments have fundamentally different rheological properties from sediment-rich environments has yet to be rigorously tested in the rock record, particularly for shallow subduction conditions. Most previous studies have focused on sediment-rich melange belts (e.g., Cloos, 1982; Cowan, 1985; Fagereng & Sibson, 2010; Fisher & Byrne, 1987; Kimura et al., 2012; Moore & Byrne, 1987) and there are few descriptions of megathrust shear zones developed in (pure) basalt, despite the hypothesis that the presence of basalt on the shallow interface may be responsible for differences in seismic and mechanical behavior. Several open questions therefore remain, including:

1. What is the role of pre-subduction alteration of basalts on subsequent deformation on the subduction interface?
2. What are the dominant deformation processes that accommodate strain in subducted basalts?
3. What role do fluid pressure and fluid content play in the subduction and deformation of basalt in the shallow, brittle regime?
4. How do the deformation processes and conditions in basalt-hosted megathrusts differ from sediment-hosted megathrusts?

In this article, we identify and describe an exhumed basalt-dominated brittle fault zone in the Chugach Complex accretionary prism in south-central Alaska. The fault zone is mappable for at least 40–50 km and is interpreted to represent a segment of the subduction megathrust. We describe the "wall rock" adjacent to the fault zone to identify alteration products and assess the role of these products in subsequent fault-related deformation. We track deformation processes within regions of different apparent strain magnitudes to determine the temporal relationships between events, and we study the composition and orientation of syn-kinematic veins to estimate the fluid content and pressure. We also examine the composition of pre-kinematic and syn-kinematic chlorite as an indication of approximate temperature of hydrothermal fluid alteration and subduction deformation. Our data indicate that the progression of basalt weakening

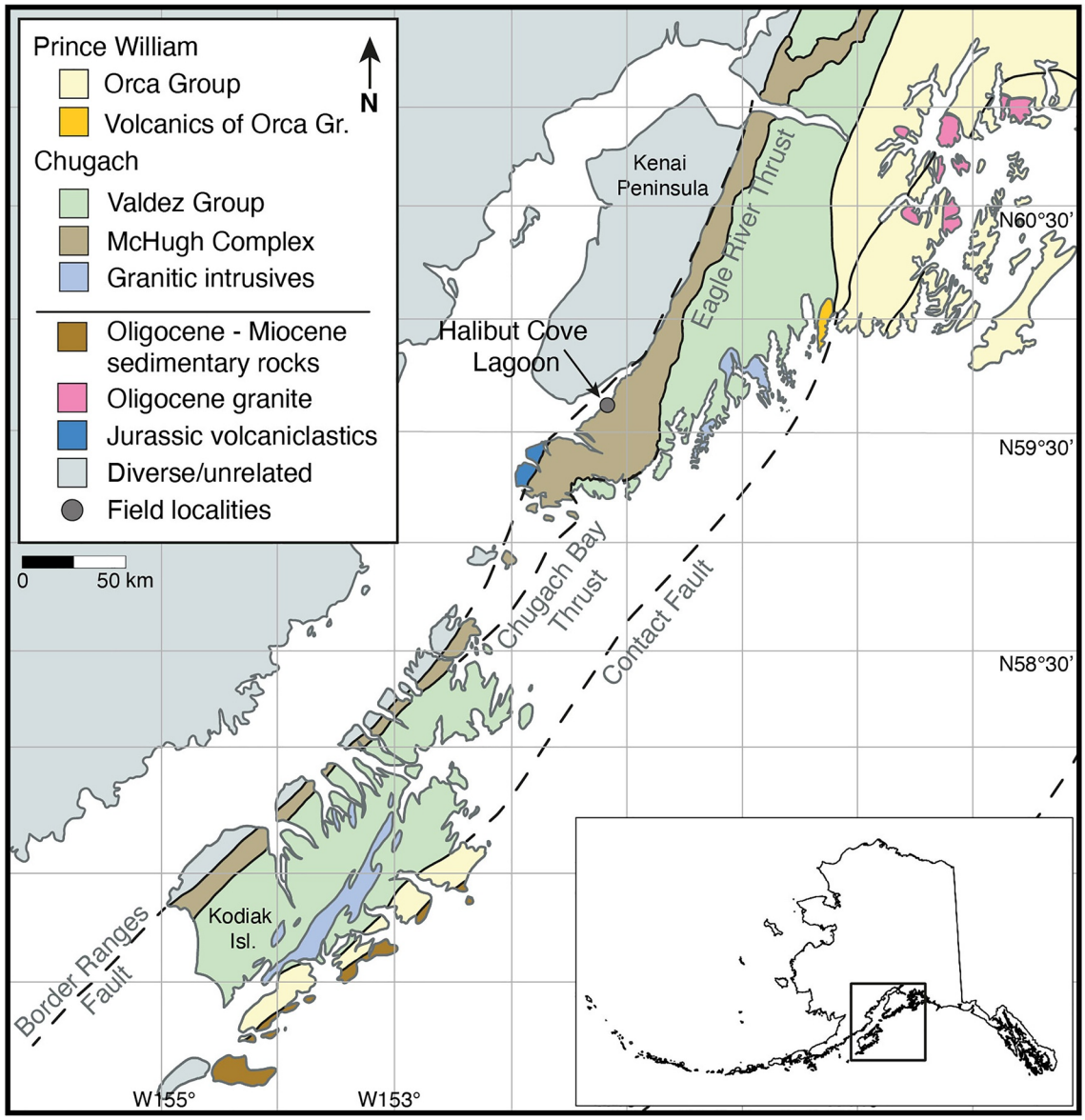

Figure 1. Map of the Chugach Complex on the Kenai Peninsula and Kodiak Island in south-central Alaska. Modified from Bradley et al. (1999). Location of study area—Halibut Cove Lagoon—indicated by gray dot.

during subduction is sensitive to pre-subduction, seafloor alteration, which lowers the frictional strength of basalt and introduces hydrous phases that contribute to syn-kinematic lithostatic pore fluid pressures (P_f) during deformation. High P_f conditions, at or above lithostatic P_f levels, are necessary to overcome the high brittle yield strength of intact basalt, but once achieved, failure progresses with lower P_f and is primarily accommodated through shearing of a chlorite-rich gouge.

2. Field Structure

2.1. Regional Geology Overview

The Chugach accretionary complex records accretion and underplating processes during subduction along the southern margin of Alaska from the mid-Mesozoic to the Cenozoic (Nokleberg et al., 1989; Plafker et al., 1989). The Chugach is exposed for over 200 km along-strike on the Kenai Peninsula (Figure 1) and is subdivided into several units composed of oceanic volcanic rocks, pelagic sedimentary rocks and trench-fill

clastic rocks, all intruded in places by Tertiary granitic plutons. The McHugh Complex represents the former accretionary wedge that formed as a result of underplating of sediments and mafic oceanic crustal rocks from the down-going plate. It is composed of a Triassic to Cretaceous meso-scale tectonic melange that contains variably deformed basalt, chert, shale, conglomerate, graywacke, and rare ultramafic rocks; it is considered the equivalent of the Uyak Complex on Kodiak Island (Bradley & Kusky, 1990; Clark, 1973). The westernmost subduction melange rocks are further subdivided into the "Potter Creek" unit based on detrital zircon ages that indicate subduction and underplating occurred from 170 to 155 Ma, compared to ca. 100 Ma for the "McHugh Creek" unit that composes the rest of the McHugh Complex (Amato et al., 2013). The Potter Creek unit is bound to the north and west by the Border Ranges Fault, which represents an original subduction thrust that was partially reactivated as a brittle strike-slip fault during the Neogene (Pavlis, 1982; Pavlis & Roeske, 2007; Figure 1). Seaward of the McHugh Complex and separated by the subduction-related Eagle River Fault, is the Valdez Group (Nilsen & Zuffa, 1982). The Valdez Group is a Cretaceous fold-and-thrust belt that formed as a result of frontal accretion during subduction and is composed of several large turbidite sequences. These turbidites reached greenschist metamorphic facies peak pressure and temperature conditions, slightly higher than the McHugh Complex (Plafker et al., 1989). The Valdez flysch is separated from sedimentary and minor mafic volcanic rocks to the south and east (Prince William Group, Figure 1) by the thrust-sense Contact Fault (Nilsen & Zuffa, 1982).

2.2. Structural Setting

The Chugach Complex on the Kenai Peninsula comprises a series of NE-SW trending thrust faults that accommodated underplating and accretion during subduction. Along some of these faults, but not all, a block-in-matrix tectonic melange of variable thickness has developed (Bradley & Kusky, 1990). These faults juxtapose mafic volcanic and sedimentary rocks from the oceanic crust, with one another and with thick slabs of massive graywacke. There is no pervasive regional tectonic foliation in the graywacke or oceanic crust units, though a spaced fabric is developed within the tectonic melange around thrust contacts (Bradley & Kusky, 1990; Kusky & Bradley, 1999). Several generations of late brittle faults cut all units. Chevron-style folded chert and shale packages are occasionally in depositional contact with pillow lava and otherwise tectonically emplaced against mafic volcanic crust. The mafic volcanic crust predominantly comprises basaltic pillow lavas and massive basalt with rare lenses of gabbro, a large ultramafic complex known as Red Mountain, and several slivers of ultramafic rocks scattered across the southern Kenai Peninsula (Kusky et al., 2007; Lytwyn et al., 2000; Figure 2). Graywacke blocks and slabs are commonly massive, with rare internal bedding indicated by gradational grain size variations. At the southwestern end of Kenai Peninsula, these fault-bounded packages of graywacke and oceanic crust are juxtaposed against blueschist-facies meta-sedimentary and meta-mafic schists of Seldovia (Bradley & Kusky, 1990; Cowan & Boss, 1978; López-Carmona et al., 2011; Figure 1).

On the southern Kenai Peninsula, several packages of underplated material are exposed in Halibut Cove Lagoon (Figure 1). These packages are predominantly derived from oceanic crust and include a thick sequence of chert, tectonic melange, repeated basalt slices, and a sliver of gabbro and ultramafic rocks (Figure 2). The timing of accretion of these assemblages is currently unconstrained, but the dominantly deep marine affinities resemble the "Potter Creek unit" of the McHugh Complex exposed along-strike in Turnagain Arm, which was accreted between 170–155 Ma. The average geothermal gradient was likely around ~20°C/km but may have been locally higher by Early Cretaceous times due to ridge subduction toward the central-west Chugach (Pavlis, 1982; Pavlis & Roeske, 2007; Rowe et al., 2009). Fluid inclusion studies suggest that rocks of the Uyak Complex were subducted to depths of 10–14 km (Vrolijk et al., 1988). The highest-grade metamorphic minerals are prehnite-pumpellyite, with only minor actinolite found in the mafic rocks, and quartz (in veins and clasts) is not substantially recrystallized. These observations suggest that these rocks reached peak temperatures of ~250°C–300°C. Throughout the early subduction history of the Chugach, the subduction interface appears to have been sediment-poor based on the abundant preservation of mid-oceanic-ridge volcanic rocks and pelagic sedimentary sequences, and the relative scarcity of marine clastics in the Potter Creek unit (Clift et al., 2012). Gaps in the detrital zircon record from underplated sediments suggests there may have been one to two periods of long-lasting subduction erosion (Amato & Pavlis, 2010; Amato et al., 2013).

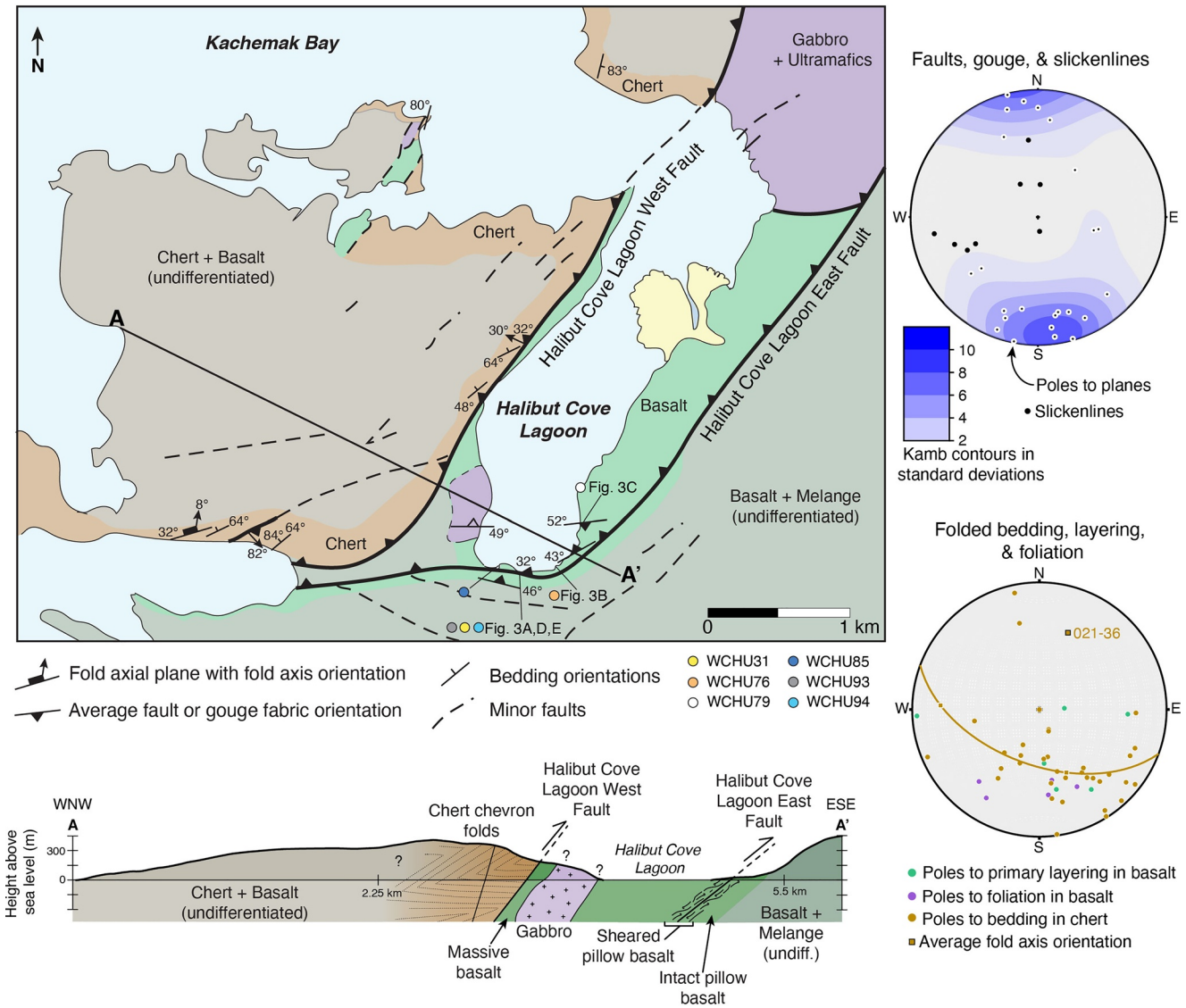

Figure 2. Geologic map and schematic cross-section of the Halibut Cove Lagoon region of the Kenai Peninsula. Some minor faults and lineaments from satellite imagery. Note vertical exaggeration on cross-section. Modified from Bradley et al. (1999). Stereonets generated using Stereonet 11; Kamb contours are for the poles to the fault and gouge planes (Allmendinger et al., 2011; Cardozo & Allmendinger, 2013).

In Halibut Cove Lagoon, there are two prominent thrust faults that cause repetitions of the oceanic crust, parallel to the underplated and accreted material exposed throughout the Chugach Complex on Kenai Peninsula (this study, Bradley et al., 1999; Bradley & Kusky, 1990). The westernmost fault, previously unnamed, places chert and basalt on top of basalt and we call it the Halibut Cove Lagoon West Fault ("West Fault"; Figure 2). The West Fault is exposed beneath the (low tide) water line in the lagoon or up along a cliff, which limits our field observations to few accessible exposures. The West Fault has folded chert in the hanging wall, a thin sliver of tectonic melange within the main shear zone, and basalt in the footwall (Figure 2). The West Fault strikes roughly parallel to the easternmost fault with a comparable dip. The chert is interbedded with shale layers a few centimeters to a few tens of centimeters thick. Open, chevron-style folding pervasively deforms the interbedded chert and shale (see lower stereonet in Figure 2) but does not affect the thrust fault. The average fold axis in the chert is plunging 36° toward the northeast. Basalt in the footwall is mostly beneath water but where exposed, the basalt is massive. Above the water line, the tectonic melange developed along the shear zone is ~1–1.5 m thick and has rounded green clasts in a dark-colored, fine-grained matrix. The easternmost fault, also previously unnamed, places basalt on top of basalt and

we call it the Halibut Cove Lagoon East Fault ("East Fault") (Figure 2). The Halibut Cove Lagoon faults cut through basalt parallel to the tectonic grain that represents the repetition of oceanic crust, rather than cross-cutting already-accreted material at a high angle. The structures in the fault zone are close to parallel to the preserved layering but slightly steeper dipping on average (Figure 2). Late upper plate deformation is observable throughout the area as brittle faults and joint sets that cut everything at a high angle. We focused our study on the East Fault as it preserves deformation localized only into basaltic units.

2.3. Outcrop-Scale Characteristics of the Halibut Cove Lagoon East Fault

The East Fault dips 60°–88° toward the west and north with an undulating fault plane. The fault forms a shear zone that is ~2 m thick with massive basalt in the hanging wall and sheared pillow lavas in the footwall (Figure 3a). The fault was previously mapped by the U.S. Geological Survey (Bradley et al., 1999) and is challenging to define precisely since there is not a single discretely developed fault plane and it places basalt on top of basalt. However, abundant field and microstructural evidence for shear deformation confirm the presence of the fault and we have delineated its location as clearly as was possible based on the degree of shearing observed (Figure 2). Flattened basalt pillows are wrapped into the shear zone along the margins of the high strain zone where basalt pillows are altered and isolated within a sheared fault gouge (Figure 3b). In lower strain zones away from the exposed fault, the host rocks comprise original seafloor pillow basalts, hyaloclastites, and massive basalts. Thick exposures of the basalt along the coastline reveal undisturbed stacked pillows with faint volcanic flow alignment and no pervasive tectonic foliation. The pillows have glassy rims, amygdales, and abundant vesicles. Hyaloclastites, or submarine brecciated basalt lava, are occasionally preserved as layers within the pillow basalts. Where abundant fault gouge has developed within the shear zone, foliation planes are defined by aligned chlorite, and occasionally epidote, in the Y shear orientation parallel to the shear plane (Figure 3c). The sheared gouge wraps the deformed and altered pillow remnants and is distinctly green in color compared to the massive black basalt and gray-green altered pillows (Figure 3d). Foliated cataclasite is present in bands that are 10–20 cm thick, generally parallel to and directly beneath the hanging wall massive basalt (Figure 3f). The foliated cataclasite is slightly coarser-grained than the sheared gouge and contains lenses of black, less-altered, basalt (Figure 3f).

3. Microstructures

3.1. Methods

Samples were collected away from the fault, in the "host rock" to examine the alteration state of intact rocks, and from four exposures of the damage zone of the East Fault, some of which capture both high- and low-strain domains that allow us to examine deformation evolution as a function of strain. One representative full thin section image of the host rock samples is shown here (WCHU79; Figure 4) and a full thin section image of the other two samples (WCHU31B and WCHU77) can be found in the Supporting Information S1. Four representative fault rock samples from the East Fault are described from least to highest relative strain (Figures 5–8); all other examined thin sections can be found in the Supporting Information S1. Two of the four fault rock samples (WCHU76 and WCHU85) were also analyzed via scanning electron microscopy (SEM) and electron-dispersive spectroscopy (EDS) at ScopeM imaging facilities (ETH Zürich). The samples were carbon-coated and analyzed using a 10 mm working distance and a 20.0 kV accelerating voltage. A compilation of relevant EDS spot analyses can be found in the Supporting Information S1.

3.2. Host Rock Samples

Outside of the shear zone, the host rock samples are composed of altered basalt pillow lavas. Intact pillows of different sizes have a smooth exterior with vesicles and amygdales concentrated around the outer rims of the pillows. There is no tectonic foliation in the host rocks and weak volcanic flow structures are present. In thin section, the host rocks have the appearance of typical basalt pillow lavas with extensive seafloor alteration (Figure 4a, see also Figures S1–S3). The groundmass is composed of randomly oriented plagioclase microlites or microphenocrysts surrounded by finer-grained feldspar and glass (Figure 4b). Round and irregularly shaped vesicles are filled with secondary (amygdaloidal) quartz, calcite, and chlorite (Figure 4a). Large, altered, euhedral plagioclase phenocrysts have small inclusions in the core (Figure 4c) and altered

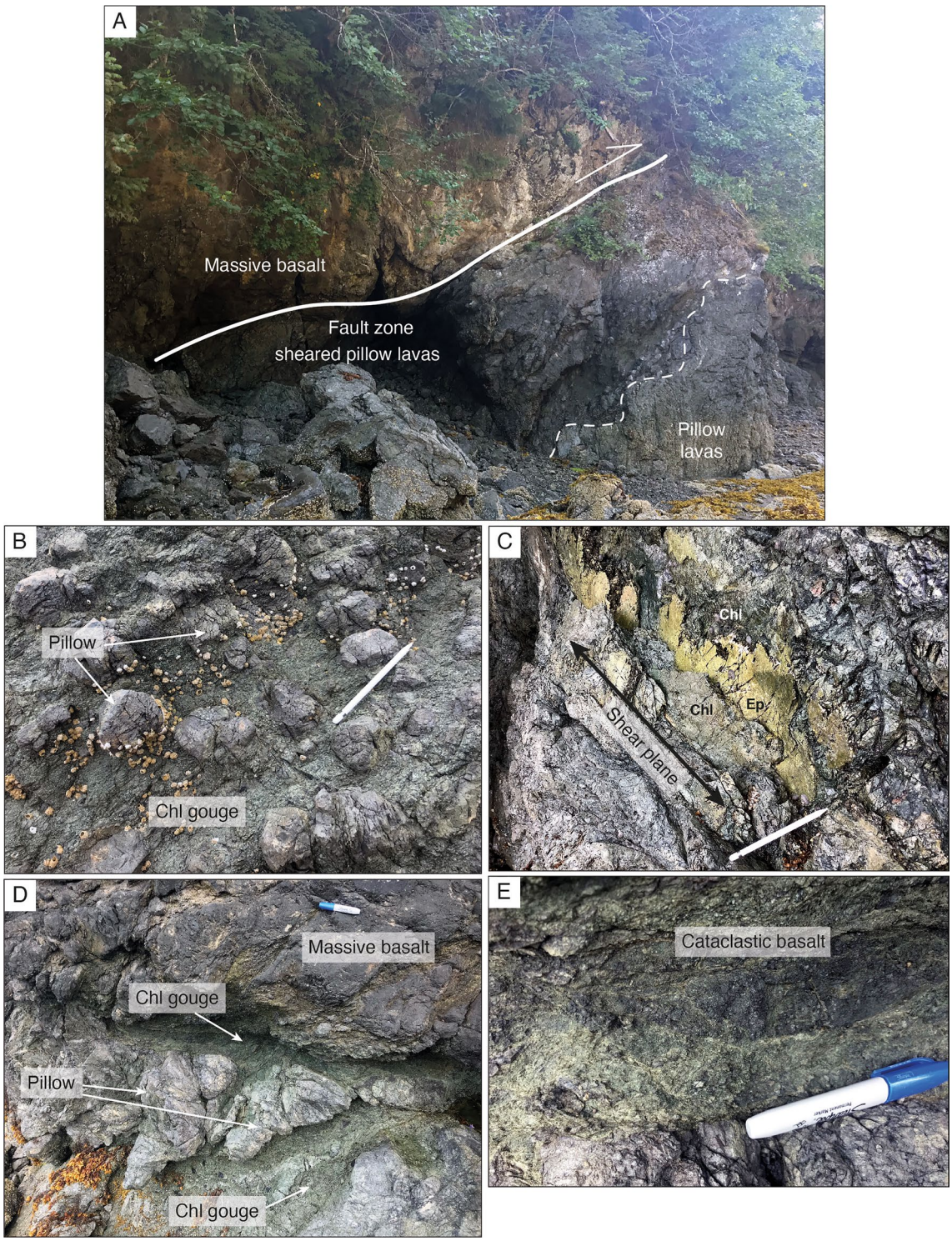

Figure 3. (a) Cross-sectional outcrop view of the basalt-hosted thrust, the East Fault, in Halibut Cove Lagoon. Pillows are flattened and sheared and isolated in a fine-grained fault gouge within several-meter-thick shear zone. Photo taken looking northeast, see Figure 2 for photo location. (b) High strain localization in basalt fault zone. Basalt pillows are becoming isolated and surrounded by sheared fault gouge. (c) Layered epidote and chlorite foliation surfaces within shear zone. (d) Chlorite-rich gouge (green) developing around relict pillows within shear zone beneath massive basalt. (e) Green and black, altered, cataclastic basalt within shear zone.

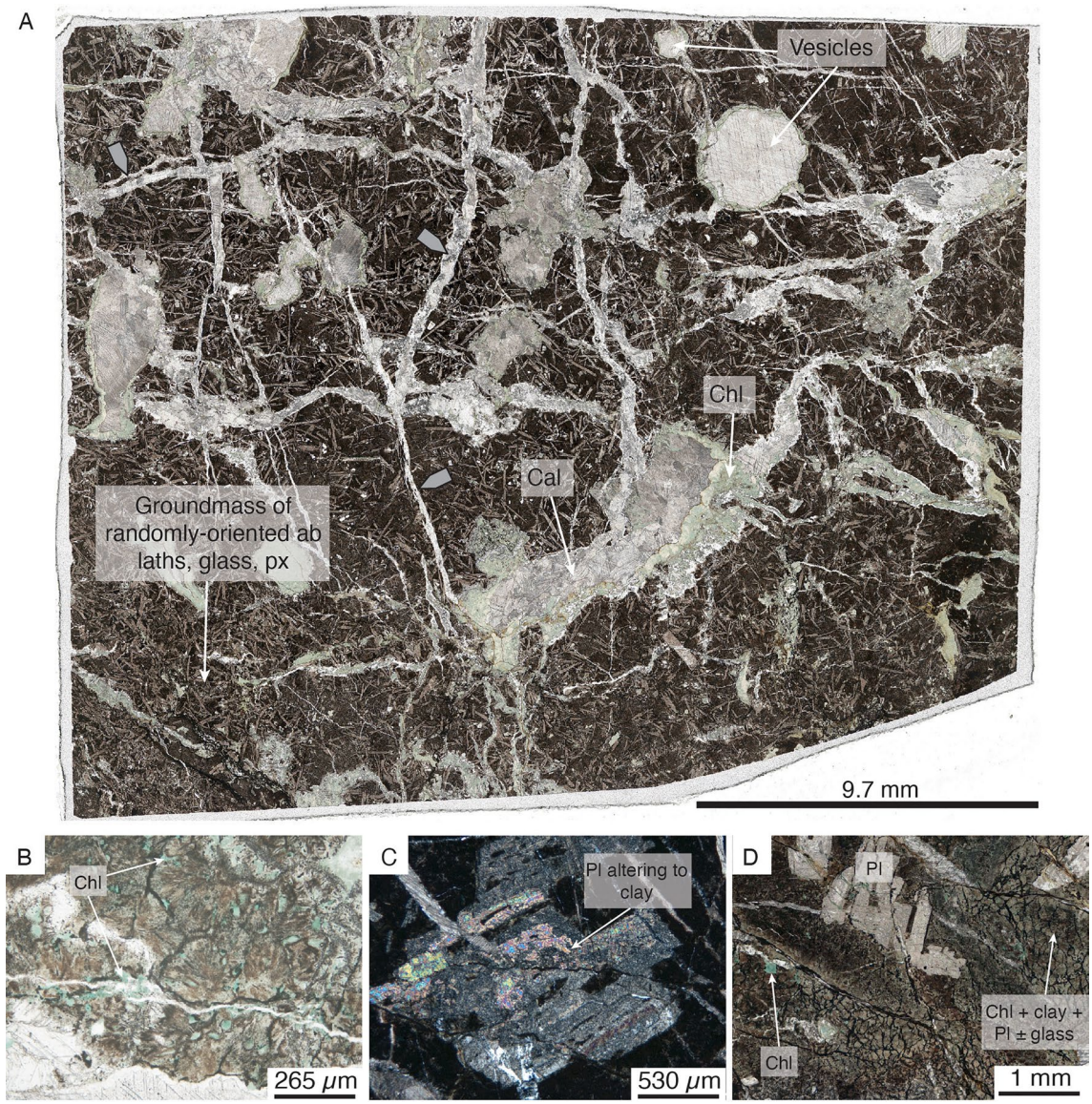

Figure 4. (a) Stitched photomicrographs of host rock sample WCHU79. (b) Abundant chlorite alteration of basalt groundmass in host rock sample WCHU31B. Note that stitched photomicrographs of host rock sample WCHU31B can be found in the Supporting Information S1. (c) Altered plagioclase phenocryst in host rock sample WCHU31B; image taken under crossed-polarized light. (d) Fractured and altered basalt groundmass in host rock sample WCHU31B. Gray arrows indicate hydrofractures (see Figure 10).

pyroxene phenocrysts are present in variable amounts. There is widespread alteration of the groundmass and phenocrysts to chlorite (Figures 4b and 4d). All host rock samples are cut through with several generations of veins that show identical secondary minerals to the vesicles. In veins and vesicles where all three secondary minerals are precipitated, quartz appears to have precipitated first (closest to the vein margins), followed by chlorite and then calcite. These veins connect the vesicles and are generally randomly oriented with some more prominent orthogonal sets (Figure 4a).

3.3. Fault Rock Samples

3.3.1. WCHU85

WCHU85 was collected from within the East Fault shear zone and captures both intact basalt and the progressive deformation of intact basalt. In hand sample, the deformed part of the sample is a green,

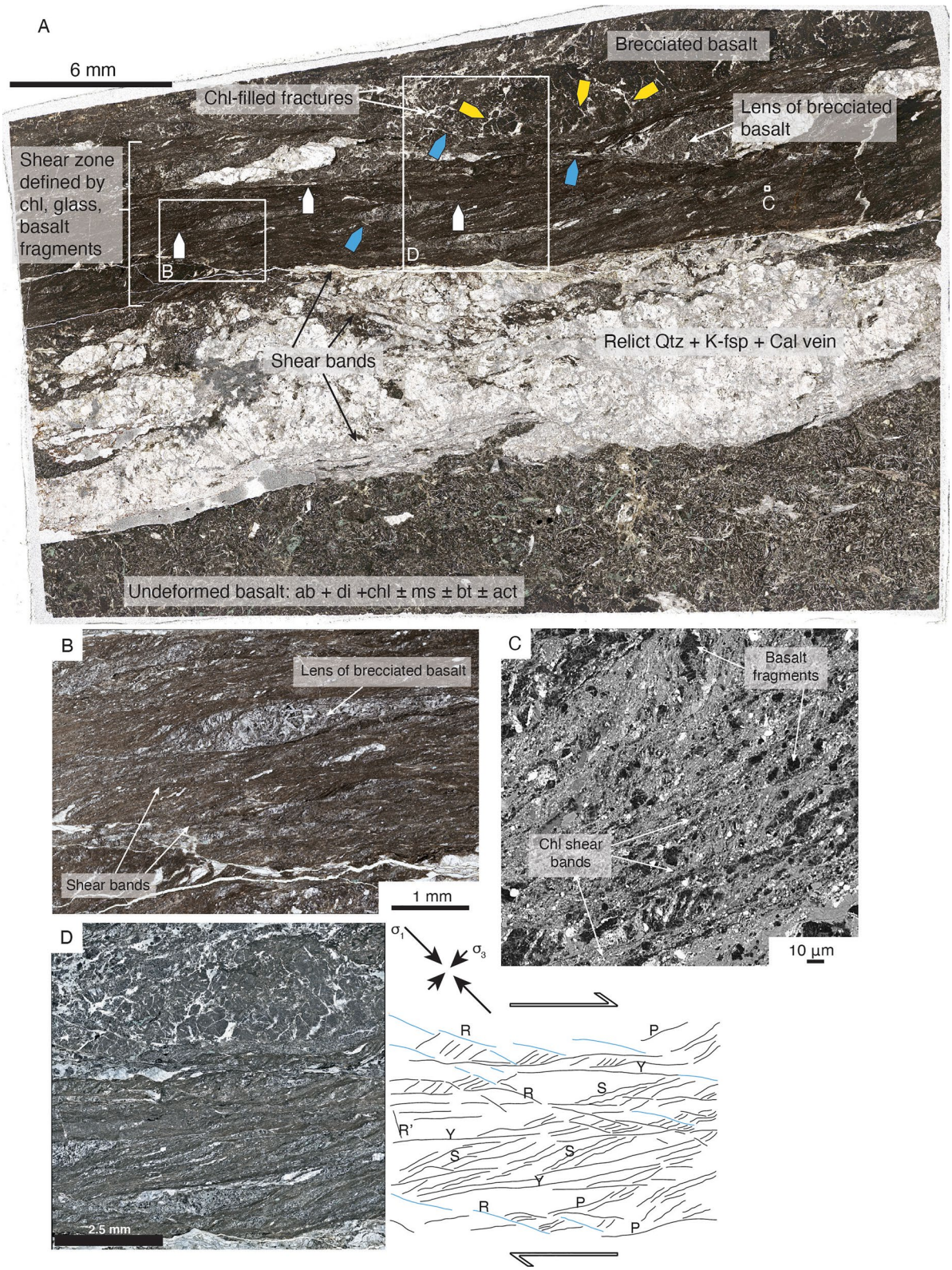

Figure 5. (a) Stitched photomicrographs of fault rock sample WCHU85. Blue arrows indicate dilatational shear fractures, yellow arrows indicate dilatational fractures, and white arrows indicate non-dilatational shear fractures (see Figure 10). (b) Chlorite shear bands defining foliation that wraps lens of brecciated basalt in fault rock sample WCHU85. (c) Backscattered electron image of cataclastic basalt fragments wrapped by chlorite shear bands. (d) Photomicrograph and interpretation sketch of sample WCHU85 showing micro-brecciated basalt that is progressively breaking down into, and wrapped by, a Riedel shear foliation.

fine-grained, and finely laminated gouge that is in direct contact with a darker green to black-colored piece of intact, less-altered, and undeformed basalt. The less-altered, intact basalt is cut by quartz-calcite veins. In thin section, the intact basalt is composed of randomly oriented plagioclase microlites and strongly altered pyroxene phenocrysts (Figure 5a). Small, round, and irregularly shaped vesicles are filled with quartz, chlorite, and calcite. A quartz-calcite-K-feldspar vein cuts through the basalt groundmass and the remainder of the section shows micro-brecciated basalt progressively developing into a strong shear fabric (Figures 5a and 5b). This vein appears to pre-date the deformation as it shows incipient foliation development at its margins and some cross-cutting shear bands. The deformed part of the thin section (upper right, Figure 5a) preserves sheared cataclasite consisting of lensoidal, micro-brecciated, and vein-rich basalt fragments of varying sizes and aspect ratios, wrapped by a fine-grained foliated gouge fabric. Larger basalt lenses preserve several generations of randomly-oriented veins filled with quartz, chlorite, and calcite, similar to the textures observed in intact host rock samples (see Section 3.2). These brecciated basalt lenses are wrapped by a brittle gouge fabric (Figures 5b–5e) defined by aligned chlorite, stretched glass fragments, and elongated ribbons of former quartz and calcite vein material (Figures 5b–5d). Several types of syn-tectonic shear bands are also developed in this part of the thin section. The intact basalt lenses both at the margins and within the gouge layer exhibit dilatational shear fractures filled with chlorite and calcite that are distinct from and crosscut the earlier, randomly oriented vein sets; they form a Riedel shear orientation (Logan et al., 1992) with respect to the surrounding shear zone boundaries (see also Figure 10d). Within the fine-grained sections of foliated fault gouge, P- and Y-shear bands also occur and are primarily occupied by smeared selvages of aligned chlorite. Chlorite shear bands are also developed along the margins of veins in a Y shear orientation and along fractures in the lower strain parts of the sample.

3.3.2. WCHU76

WCHU76 samples the margin of a basalt pillow that grades into a strongly sheared cataclasite from within the East Fault shear zone. In hand sample, abundant small vesicles and amygdales are visible on the side of the sample that is intact basalt. The intact basalt is wrapped by a dark green to green-colored, fine-grained fault gouge. In thin section, these same two zones, intact basalt and sheared fault gouge, are also visible along with a gradational zone between them (Figure 6a). One side of the thin section (Zone 1 in Figure 6a) shows nearly undeformed basalt with a very-fine-grained, glassy groundmass and abundant, small, round vesicles that are filled with secondary minerals quartz, minor chlorite, and calcite. The basalt groundmass is composed of fine-grained, dendritic feldspar microlites, and slightly larger plagioclase laths that are primarily albitic in composition with some relict Ca-zoning in the cores of larger grains. Reaction textures on the margins of larger plagioclase laths show a Ca-rich component exsolving out of the grain (see Supporting Information S1). The plagioclase laths, including the surrounding reaction textures, have significant compositional impurities of Mg and Fe and traces of P, Fl, S, Ti, and K. A single set of conjugate veins, similarly filled with early quartz followed by calcite, cut the groundmass, phenocrysts, and connect the vesicles (Figure 6a). A smaller set of later en echelon veins are developed along the margin of this vesicular pillow basalt near its contact with sheared basalt (Figure 6b). All of these microstructures are consistent with features observed in the intact host rock samples.

The rest of sample WCHU76 is composed of zones of micro-brecciated basalt (Zone 2 in Figure 6a), cataclasite (Zone 3 in Figure 6a), and ultracataclasite (Zone 4 in Figure 6a). The micro-brecciated basalt zone contains basalt that has been extensively fractured but lacks pervasive shear. The basalt fragments are angular nearest the intact Zone 1 basalt and become progressively subangular to weakly rounded toward the middle of the thin section next to the cataclastic zones. The fractured, partial remains of vesicles are visible within some brecciated basalt fragments. Chlorite fills most fractures and the fractures are dominantly oriented approximately orthogonal to the ultracataclasite zones that border the micro-brecciated portion of the thin section. Two lenses of former vein material (quartz and feldspar) are wrapped and overprinted by chlorite shear bands within the brecciated basalt zone.

Two sections of cataclasite (Zone 3) make up the majority of the thin section at the opposite end to the intact basalt. The cataclastic zones contain a fine-grained matrix that wraps lenses of brecciated basalt and former vein material. The cataclasite matrix is composed of small fragments of plagioclase (variable

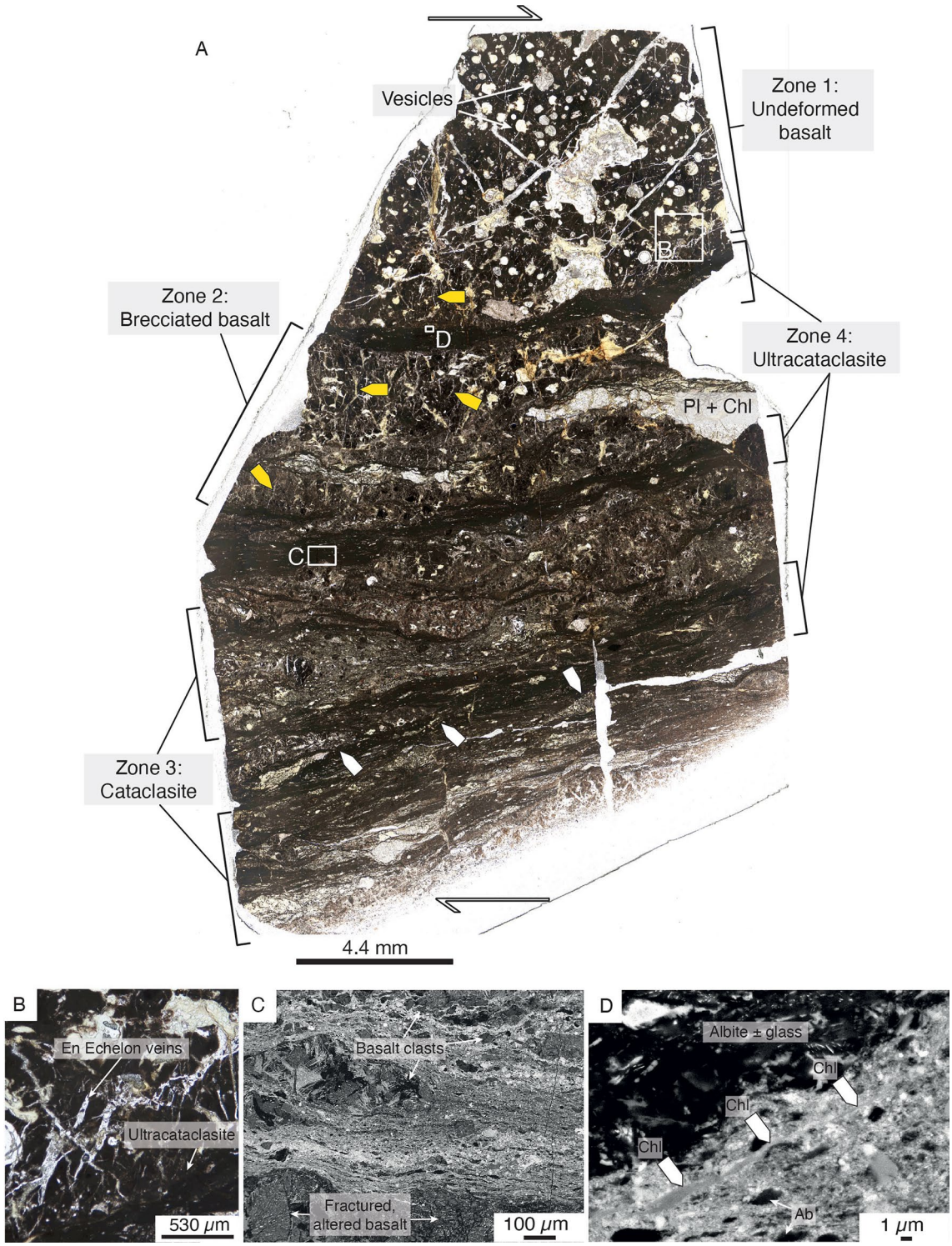

Figure 6. (a) Stitched photomicrographs of fault rock sample WCHU76, see text for description of zones. (b) En echelon veins filled with quartz and chlorite in basalt fault rock sample WCHU76. (c) Backscattered electron image of ultracataclasite zone in basalt fault rock sample WCHU76. (d) High magnification backscattered electron image of utracataclasite zone showing long thin growth of chlorite parallel to the shear plane in the ultracataclasite matrix (white arrows). Yellow arrows indicate dilatational fractures and white arrows indicate non-dilatational shear fractures (see Figure 10).

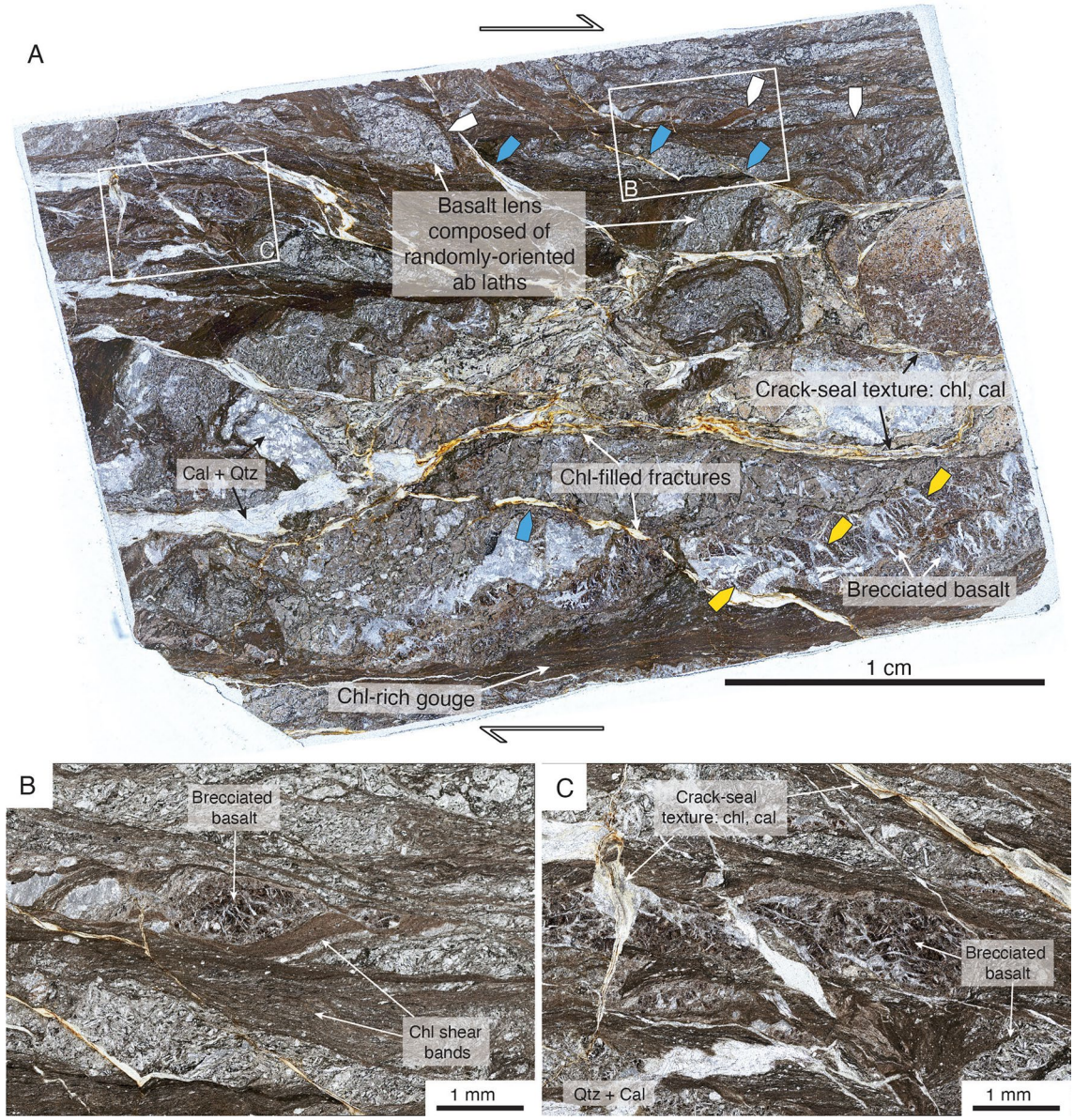

Figure 7. (a) Stitched photomicrographs of fault rock sample WCHU93. Image rotated to orient Y shears approximately horizontal. (b) Lens of intact, fractured basalt wrapped by a sheared gouge fabric in fault rock sample WCHU93. (c) Brecciated basalt wrapped by chlorite-rich gouge that is cut by syn-kinematic fluid-filled fractures in fault rock sample WCHU93. Blue arrows indicate dilatational shear fractures, yellow arrows indicate purely tensile fractures, and white arrows indicate non-dilatational shear fractures (see Figure 10).

Na and Ca content), albite, chlorite, epidote, titanite, apatite, and minor pyrite (Figure 6c). The only fractures visible in Zone 3 are those that are preserved within clasts or fragments of basalt; fractures do not cut the cataclastic matrix. Clasts of former vein material have been sheared into lensoidal shapes with thin elongated tails that run parallel to the cataclastic foliation. Lenses of patchy, brown-colored rock show the progression of fractured basalt fragments breaking down into a fine-grained cataclastic matrix. Within these patchy zones, the shapes of basalt fragments are still visible but the basalt shows evidence for breakdown and boudinage and chlorite fills the spaces between fragments. These zones are wrapped by very fine-grained cataclastic material, and although the fine grain size makes it difficult to identify exact mineral proportions, the brightness observed under backscatter electron imaging suggests these zones are dominated by chlorite and oxides.

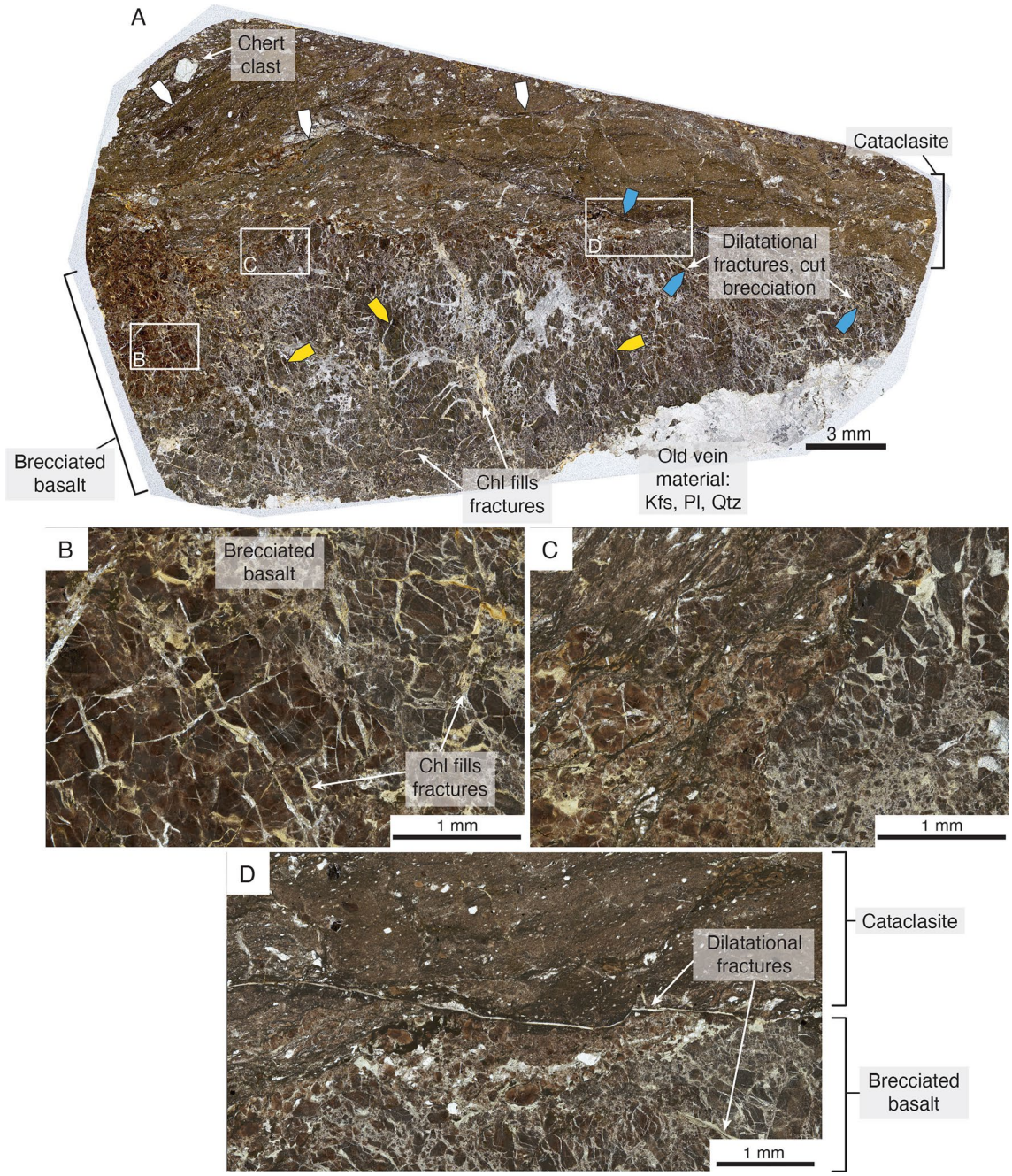

Figure 8. (a) Stitched photomicrographs of fault rock sample WCHU94. (b) Micro-brecciated basalt with chlorite-filled fractures. (c) Fragments of basalt being plucked off margin of brecciated basalt zone and incorporated into the cataclastic zone. (d) Dilatational fractures filled with chlorite cut the cataclasite and brecciated basalt. Blue arrows indicate dilatational shear fractures, yellow arrows indicate dilatational fractures, and white arrows indicate non-dilatational shear fractures (see Figure 10).

Three narrow zones of ultracatclasite (Zone 4) separate the intact basalt (Zone 1) from the brecciated basalt (Zone 2) and separate sections of cataclasite (Zone 3; Figure 6a). The ultracataclasite is a much finer-grained version of the Zone 3 cataclasite and necessitates SEM imaging to observe the components. The ultracataclasite matrix is also composed of plagioclase (variable Na and Ca content), albite, chlorite, epidote, titanite, apatite, and minor pyrite (Figure 6c), each exhibiting much finer grain sizes compared to the cataclasite zones. In the largest clasts remaining in the ultracataclasite zones, basalt fragments containing older, chlorite-filled fractures are visible. Ribbon-like lenses elongated parallel to cataclasite fabric are composed of

plagioclase; EDS spot analyses confirm that these lenses have two discrete components: an inner, fractured grain, that is, mixed Ca-Na plagioclase and that is surrounded by a darker lens of nearly pure albite. Chlorite and occasionally epidote form elongated grains within the cataclastic fabric parallel to the cataclastic zone boundaries and shear plane (Figure 6d). No discrete fractures are visible within, or cut, these higher-strain ultracataclasite zones.

3.3.3. WCHU93

WCHU93 samples a distinct lens of cataclastic fault gouge from within the East Fault shear zone; the sample is cut parallel to slickenlines that wrap the basalt lens. In hand sample, a mottled green and black cataclastic exterior wraps many smaller, sheared lenses of gouge and intact basalt fragments, all of which are fractured. In thin section, the sample shows a fine-grained, clay- and chlorite-rich sheared gouge foliation that wraps blocks and lenses of intact basalt (Figures 7a and 7b). The basalt lenses in this fault rock have the same texture as the host rock samples with randomly oriented feldspar phenocrysts in a fine-grained glassy groundmass (see also intact basalt Zone 1 of sample WCHU76). The basalt lenses appear to be breaking down during cataclasis and are disaggregating directly into fault gouge (Figure 7b). Some of the basalt blocks are breccia fragments with fractures filled with quartz and calcite, comparable to the micro-brecciated Zone 2 basalt of sample WCHU76. These fractures cut only the basalt and do not extend into the cataclastic gouge foliation that wraps the basalt blocks. These blocks, and the gouge fabric, are cut by a set of later fractures that are filled with calcite and chlorite and cut parallel to the *R'* direction (Figures 7a and 7c). The chlorite in these late syn-kinematic veins is fibrous with a crack-seal texture that records early chlorite and later calcite and quartz fill. These hybrid extensional-shear chlorite fractures post-date the chlorite-rich gouge fabric, which is offset along the fractures. The chlorite (and clay and glass) gouge coalesces into shear bands that wrap lenses of basalt and brecciated basalt.

3.3.4. WCHU94

Sample WCHU94 samples cataclastic fault gouge from within the East Fault shear zone. In hand sample, two distinctly different zones are observable. A black, finely fractured clast that contains felsic material in the fractures is wrapped by a green-colored, fine-grained gouge. In thin section, half of the sample is composed of micro-brecciated basalt and the other half of the sample is composed of sheared cataclasite (Figure 8). The basalt micro-breccia is nearly identical to Zone 2 of sample WCHU76 with quartz-, calcite-, and chlorite-filled fractures that are oriented orthogonal to the shear plane of the cataclastic zone (Figures 8a and 8b). These fractures do not cut the cataclasite. The brecciated basalt fragments are smaller and slightly more rounded along the border with the cataclastic zone. Dilatational *R* shears filled with chlorite cut the micro-brecciated basalt and have a crack-seal texture that indicates repeated opening of the same fracture (Figure 8d). The cataclastic portion of the sample contains a fine-grained, sheared gouge foliation with clasts of fractured basalt, feldspar, and rare clasts of chert. Several chlorite-filled dilatational *R* shears also cut the cataclasite (Figure 8d). Patchy brown lenses of basalt, similar to those observed in Zone 3 of sample WCHU76, are wrapped by, and breaking down into, the gouge fabric. Along the border between the micro-brecciated basalt and the cataclasite, clasts/fragments of basalt are being plucked off the margin of the micro-brecciated zone and incorporated into the cataclastic shear zone (Figures 8a, 8c and 8d).

4. Composition

4.1. Methods

To determine the quantity and composition of clay and phyllosilicate minerals formed syn-kinematically during subduction deformation, X-ray diffraction (XRD) analyses were carried out on five randomly oriented powder specimens (three cataclastic fault rocks and two host rock basalts) at the Clay Lab of ETH Zürich. First, the sample was crushed with a jaw breaker <0.4 mm and homogenized. A representative aliquot split of 2 g was milled in ethanol to a grain size below 20 μm with a McCrone micronizing mill. After drying at 65 C the material was ground using a mortar and pestle, and then sieved directly onto the sample holder through a 200 μm sieve. A blade was used for packing, sample-height adjustment, and forming a flat surface

Table 1
XRD Results for Two Host Rock Basalt Samples and Three Deformed Fault Rock Samples

	WCHU79		WCHU85		WCHU85		WCHU76		WCHU93	
	Host rock		Host rock		Cataclasite		Ultracataclasite		Cataclasite	
Mineral	wt%	3σ	wt%	3σ	wt%	3σ	wt%	3σ	wt%	3σ
Quartz	5.2	0.2	9.0	0.3	6.6	0.2	3.2	0.2	8.6	0.4
K-feldspar	2.2	0.4	5.4	0.4	11.0	0.5	5.6	0.4	5.5	0.6
Na-plagioclase	38.8	0.7	29.6	0.5	22.7	0.6	26.6	0.8	25.8	0.8
Calcite	13.5	0.3	4.2	0.2	3.3	0.2	3.1	0.4	9.4	0.3
Actinolite			0.4	0.2	0.4	0.1				
Diopside			11.6	0.5	9.5	0.5				
F-apatite	1.0	0.2	1.0	0.2	1.5	0.2	1.6	0.2	0.8	0.1
Titanite	7.1	0.4	7.5	0.4	8.7	0.5	8.9	0.5	7.2	0.5
Total non-clay	67.8		68.7		63.7		49.0		57.3	
Illite (dioctahedral mica)	8.1	0.4	1.0	0.3	1.3	0.2	24.7	0.4	10.3	0.9
Biotite (trioctahedral mica)	5.0	1.1	3.1	0.3	3.9	0.4				
Chlorite/smectite (ml)			3.9	0.5						
Chlorite (trioctahedral)	19.1	0.8	23.4	0.8	31.1	1.1	26.3	1.0	32.4	1.5
Total clay/phyllosilicate	32.2		31.4		36.3		51.0		42.7	
Total identified	100.0		100.1		100.0		100.0		100.0	

Note. Sample WCHU76 contains results from both ultracataclasite and cataclasite material since they were too fine-grained to separate.

(Zhang et al., 2003). A second sample preparation procedure was used to produce oriented specimens for enhancement of the basal reflexes of layer silicates. Changes in the reflex positions by intercalation of different organic compounds (e.g., ethylene glycol) and after heating were used for identification in part of smectite.

XRD measurements were conducted using a Bragg-Brentano diffractometer (Bruker AXS D8) and Co-Kα radiation. The diffractometer is equipped with an automatic q-compensating divergence slit and anti-scatter screen for dynamic beam optimization, with primary and secondary soller slits and a LynxEye XE-T line detector. Samples were scanned at room temperature at a step width of 0.022θ (1 s per step) from 2.5 to 802θ. The composition was qualitatively determined using the software DIFFRAC.Eva v.4.3.0 (BRUKER AXS). Mineral phases were assigned based on peak position and relative intensity compared to the PDF-2 database (International Center for Diffraction Data). Finally, the overall bulk rock mineral composition was quantitatively determined by Rietveld analysis using the Rietveld program Profex v4.1.0 (Doebelin & Kleeberg, 2015).

The composition of chlorite in host rock sample WCHU31B and fault rock sample WCHU85 was determined via electron microprobe at ETH Zürich. The samples were carbon-coated and analyzed using a 20 nA beam current and 5 μm diameter beam size. Several points were analyzed for each chlorite domain of interest and a complete table of the chlorite analyses can be found in the Supporting Information S1.

4.2. XRD Results

Results of XRD analysis are reported in Table 1 and Reitveld fits for each of the analyzed samples can be found in the Supporting Information S1. Two host rock basalt samples, WCHU79 and the undeformed portion of WCHU85, contain between 30%–39% Na-plagioclase, 19%–23% chlorite, and 1%–8% illite (dioctahedral mica). Three cataclastic fault rock samples, WCHU76, WCHU93, and the deformed portion of WCHU85, contain between 23%–27% Na-plagioclase, 26%–32% chlorite, and 1%–25% illite. Based on the relatively low illite content in the host rock samples, a significant portion of the illite likely grew syn-kinematically during

subduction deformation. Sample WCHU76 contains both ultracataclasite and cataclasite because the ultracataclasite occurs in bands that are too fine-grained to reliably separate. All identified dioctahedral mica was interpreted to be illite. There is some uncertainty in the exact quantity of dioctahedral and trioctahedral mica, which proved difficult to identify in small quantities. Where trioctahedral mica was identified in larger quantities than 5 wt% via XRD for samples that did not have any apparent biotite (verified by petrography and SEM analysis), it was added to the dioctahedral total. All samples contain minor amounts of quartz, calcite, actinolite, fluoroapatite, titanite, diopside, chorite-smectite, and relic biotite (trioctahedral mica). Quartz and calcite and K-feldspar are interpreted to reflect the veins that cut all samples. There is between 36% and 51% total clay (chlorite-smectite) and phyllosilicate (including chlorite, illite, and relict biotite) content in the cataclastic gouge. Total clay and phyllosilicate content is highest in sample WCHU76, which is the only sample that contains layers of both cataclasite and ultracataclasite and suggests that chlorite and illite content increase progressively with comminution and strain localization during basalt deformation.

4.3. Chlorite Composition Results and Thermometry

Chlorite from host rock sample WCHU31B has slightly lower Si, higher Al, higher Fe^{2+}, and lower Mg compared to chlorite from the fault rock sample WCHU85. The analyzed chlorite compositions correspond to two different microstructural settings that are interpreted to record chlorite growth at different temperature conditions: pre-subduction hydrothermal growth (sample WCHU31B) and later, syn-kinematic growth during subduction (sample WCHU85). In an attempt to quantify these temperature differences, we applied the low temperature chlorite thermometer of Bourdelle et al. (2013). This chlorite thermometer considers all Fe to be Fe^{2+} and considers chlorite compositions to be ideal; that is, there is no tetrahedral Ti, no octahedral Mn, and no K, Na, Ca contamination ($Na + Ca + K < 0.2$; Bourdelle & Cathelineau, 2015; Bourdelle et al., 2013; Potel, 2007). An ideal chlorite composition is justified for the Halibut Cove lagoon samples because they contain only minor traces of Ti, Mn, K, Na, and K. Plotting these results on a graphical representation of the low temperature chlorite thermometer yields relatively higher temperatures of formation for the host rock chlorite compared to the syn-kinematic fault rock chlorite (Figure 9). The chlorite compositions are marginal to the window of optimal reliability defined for the low-temperature chlorite thermometer ($1.5 < R^{3+} < 3.5$ atoms per formula unit; Bourdelle & Cathelineau, 2015; Bourdelle et al., 2013), probably since the chlorite is a result of hydrothermal circulation (and syn-kinematic recrystallization of hydrothermal chlorite) rather than pure diagenetic processes. Due to the less-than-optimal application of the thermometer, we do not emphasize the absolute temperatures obtained but note that the thermometer suggests chlorite growth at different temperature conditions as a function of microstructural domain.

5. Interpretations

5.1. The Pre-Subduction Alteration State of Halibut Cove Lagoon Basalts

The Halibut Cove Lagoon samples show strong evidence for hydrothermal seafloor alteration prior to subduction. This includes the presence of abundant albite rather than the calcium-rich anorthite expected in seafloor basalts. Albitization is a common process in which circulating hydrothermal fluids cause sodium to replace calcium in plagioclase feldspar (Alt et al., 1986; Honnorez, 2003; Humphris & Thompson, 1978; Perez, 2005; Rosenbauer et al., 1988). Direct evidence of this reaction can be observed in sample WCHU76, in which the Ca-component is visibly exsolved from the Na-rich feldspar component along the margins of feldspar phenocrysts (see Supporting Information S1). The albitization process generally occurs in the presence of excess silica at around 350°C and produces chlorite and smectite (Rosenbauer et al., 1988), consistent with the observation that clays and sheet silicates compose around 30% of host rock and weakly deformed samples. This interpretation is further supported by contrasting chlorite compositions preserved in undeformed and deformed samples (see Section 4.3). Chlorite composition from undeformed sample WCHU31B is more Fe^{2+}-rich and Mg-poor compared to syn-kinematic, deformed chlorite from sample WCHU85. These chlorite compositions, when evaluated with a low-temperature chlorite thermometer (Bourdelle & Cathelineau, 2015; Bourdelle et al., 2013), yield a higher temperature of formation for the undeformed sample and a lower temperature of formation for the deformed sample (see Figure 9). Thus the data indicate an early stage of chlorite growth resulting from hydrothermal fluid reactions on the seafloor, followed by lower-temperature syn-kinematic chlorite production during shallow subduction deformation.

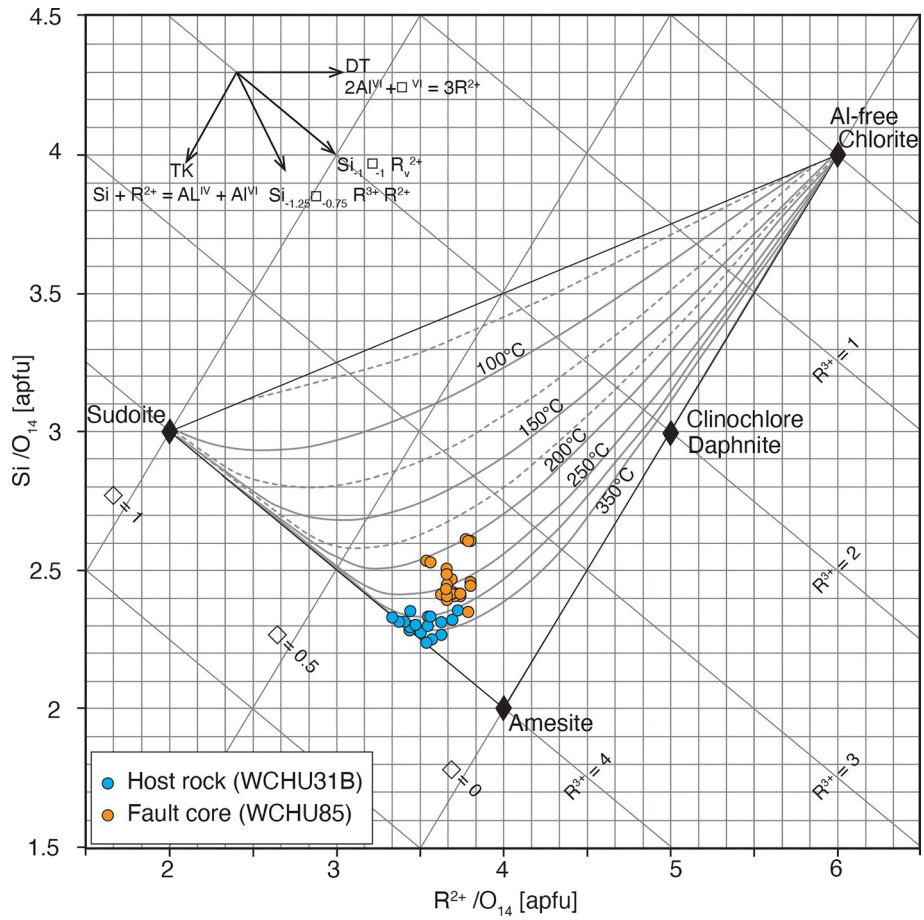

Figure 9. Chlorite compositions from host rock sample WCHU31B and fault rock sample WCHU85 plotted on the graphical thermometer of (Bourdelle & Cathelineau, 2015) and and the R^{2+}—Si diagram of Wiewióra and Weiss (1990). Note that $R^{2+} = Mg^{2+} + Fe^{2+}$ and $R^{3+} = (28 - 2R^{2+} - 4Si)/3$. Solid gray lines represent 50°C temperature increment and dashed lines represent 25°C temperature increments. □ represents vacancies/empty octahedral sites in the structure of chlorite. All data were normalized to 14 oxygens. Apfu: atoms per formula unit.

5.2. Deformation Progression Preserved in Halibut Cove Lagoon Samples

A combination of early alteration, fracture, cataclasis, and shear band development define the fault rock samples of Halibut Cove Lagoon. Based on the microstructures documented in this study, we interpret there to have been several phases of deformation and mineralogical changes involved in weakening these basalts during shallow subduction, as outlined below.

1. Phase 1: First, hydrothermal seafloor alteration produced weaker phases (chlorite) such that deformation could eventually localize more easily than in unaltered basalts. Without moderate seafloor alteration, basalt contains few hydrous minerals (e.g., biotite and amphibole) and in relatively low abundance.
2. Phase 2: Extensive hydraulic fracturing broke up the basalt into fragments and quartz, chlorite, and calcite-filled fracture spaces. The presence of crack-seal textures in these fractures and multiple generations of them suggest that this early fracture process was cyclical and that fluid compositions fluctuated through time.
3. Phase 3: During the very earliest stages of subduction-related deformation, pre-fractured basalt fragments were further brecciated, weakly boudinaged and cut by en echelon tensile and hybrid extensional shear fractures oriented at high angles to the shear plane. Some samples also developed sets of dilatational fractures in an orientation consistent with Riedel shears. In all fault rock samples, an early flux of siliceous fluid was followed by a carbonaceous fluid flux, all of which is repeated at least twice, while chlorite appears to have crystallized both prior to and after the carbonaceous fluid. With increasing

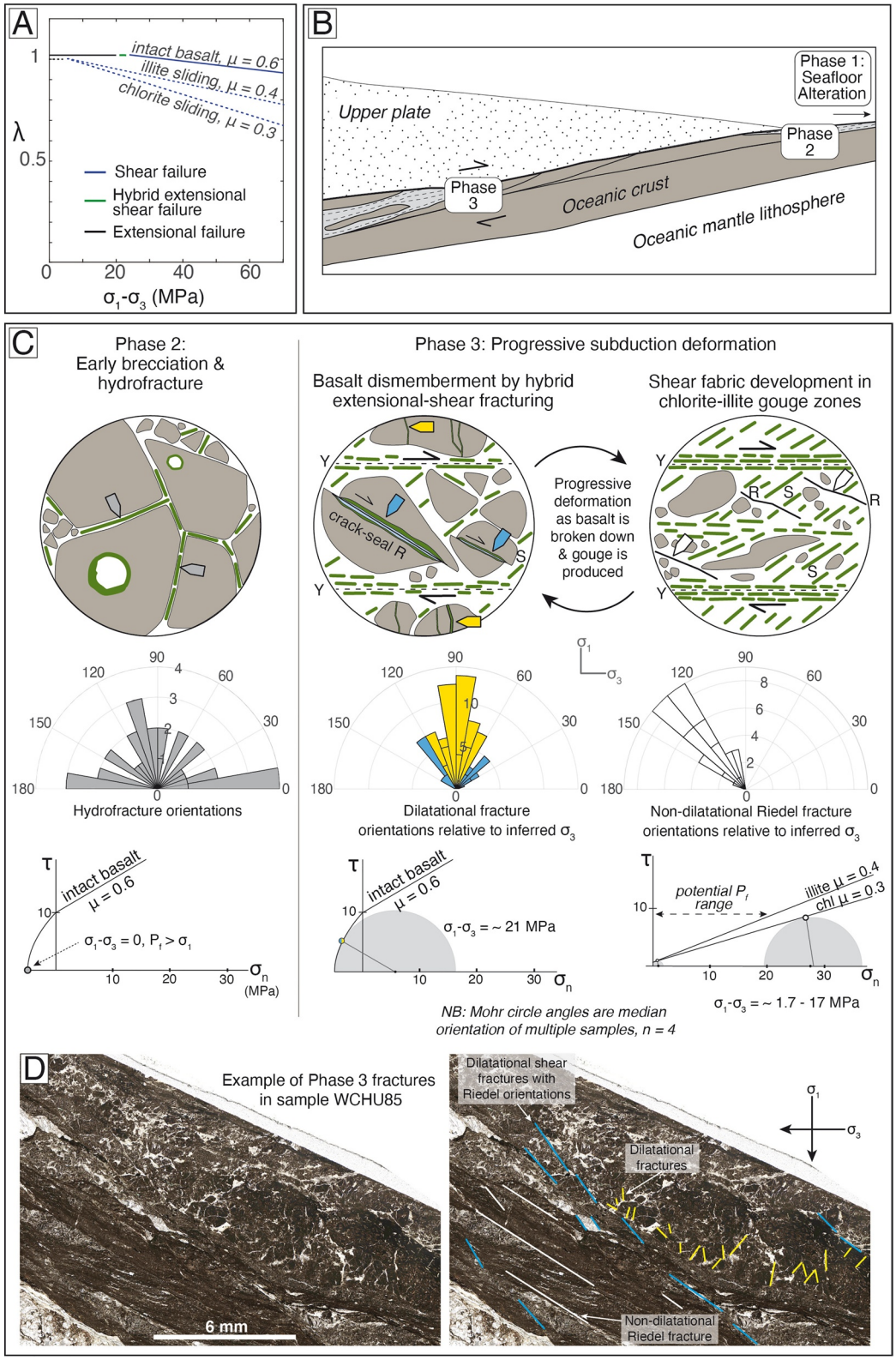
A
intact basalt, μ = 0.6
illite sliding, μ = 0.4
chlorite sliding, μ = 0.3
λ
Shear failure
Hybrid extensional shear failure
Extensional failure
σ1-σ3 (MPa)
B
Phase 1: Seafloor Alteration
Upper plate
Phase 2
Phase 3
Oceanic crust
Oceanic mantle lithosphere
C
Phase 2: Early brecciation & hydrofracture
Phase 3: Progressive subduction deformation
Basalt dismemberment by hybrid extensional-shear fracturing
Shear fabric development in chlorite-illite gouge zones
crack-seal R
Progressive deformation as basalt is broken down & gouge is produced
Hydrofracture orientations
Dilatational fracture orientations relative to inferred σ3
Non-dilatational Riedel fracture orientations relative to inferred σ3
intact basalt μ = 0.6
σ1-σ3 = 0, Pf > σ1
σ1-σ3 = ~ 21 MPa
potential Pf range
illite μ = 0.4
chl μ = 0.3
σ1-σ3 = ~ 1.7 - 17 MPa
NB: Mohr circle angles are median orientation of multiple samples, n = 4
D
Example of Phase 3 fractures in sample WCHU85
6 mm
Dilatational shear fractures with Riedel orientations
Dilatational fractures
Non-dilatational Riedel fracture

Figure 10.

strain, thin bands of cataclastic deformation began to wrap the coarse, fractured lenses of basalt and to coalesce into wider zones of cataclasis, forming a distinctive gouge. During cataclastic flow, the rotation and sliding of basalt fragments past one another caused granulation or fragmentation into progressively smaller fragments (comminution). Chlorite, illite, and minor epidote accommodated grain sliding during cataclasis and formed thin, elongate grains aligned parallel to the shear orientation. Earlier vein material within the basalt was strung out into thin cataclastic ribbons by this process, which, combined with aligned chlorite aggregates, define a strong cataclastic foliation. This process eventually resulted in the development of ultracataclasite that is so fine-grained that the components are only identifiable via SEM (e.g., sample WCHU76, see Figure 6). As deformation progressed, chlorite was concentrated as albite broke down and new syn-kinematic chlorite and illite were produced, such that deformation was predominantly taken up by slip on sheet silicates and in some samples, this resulted in chlorite shear bands (Y shears) oriented parallel to the shear plane.

5.3. Interpreted Mechanical Evolution

The differential stress and pore fluid pressure (P_f) conditions associated with each phase in the microstructural progression described in Section 5.2 can be bracketed if we make some assumptions about basalt and basalt-derived gouge frictional properties based on laboratory experiments. The frictional strength of intact mafic volcanic rocks has been estimated from experiments on unaltered basalt, gabbro or gabbro gouge, feldspar gouge, and altered basalt, all of which have coefficients of friction (μ) approximately consistent with Byerlee's law of $\mu = 0.6–0.7$ at low temperatures (100°C–400°C; He et al., 2007; Masuda et al., 2019; Phillips, Belzer, et al., 2020; Zhang et al., 2017). In comparison, potential gouge components have lower friction coefficients based on experiments conducted at low temperatures: For example, wet chlorite ($\mu = \sim 0.3$), wet illite ($\mu = \sim 0.4$), and wet smectite ($\mu = 0.1–0.2$; Behnsen & Faulkner, 2012; Okamoto et al., 2019). Based on the microstructures described, the Halibut Cove Lagoon rocks can be divided into two end-members: intact altered basalt fragments ($\mu = 0.6$), and chlorite-dominated cataclastic layers ($\mu = 0.3$). We assume the intact basalt has a tensile strength of 5 MPa (Perras & Diederichs, 2014) and experiments suggest that cohesion in clay-rich fault gouges is less than 0.5 MPa and we use this value as a conservative maximum (Ikari & Kopf, 2011; Insua-Arévalo et al., 2021). The vertical stress (σ_v) is assumed to be parallel to σ_3 and is calculated for an overburden density of 2,500 kg/m^3 and a depth of 10 km (consistent with the subduction depth suggested for the correlated Uyak Complex Vrolijk et al., 1988).

In Figure 10, we summarize the main phases of basalt deformation (Phases 2 and 3 discussed in Section 5.2 and shown schematically in Figures 10b and 10c) recorded in the Halibut Cove Lagoon samples, along with interpreted mechanical conditions in which they formed. Figure 10a is a failure mode diagram following Cox (2010) that shows the failure curves for chlorite- and illite gouge and intact basalt for a range of differential stresses and pore fluid factors (λ). The Mohr circle diagrams in Figure 10c show the same information, but also include the median orientations of fractures measured in four samples for each deformation phase. Fracture orientations are summarized in the rose diagrams in Figure 10c for Phases 2 and 3 deformation. Thin section images annotated with measured fracture orientations can be found in the Supporting Information S1 and an example is shown in Figure 10d. The reference frame for the fracture orientations was established by assuming that σ_3 was oriented approximately perpendicular to purely extensional fractures.

Figure 10. (a) Failure mode diagram after (Cox, 2010) illustrating the stress state of the Halibut Cove Lagoon fault rocks during hybrid extensional-shear failure of the dilatational Riedels and slip on compressional chlorite S surface. (b) Schematic representation of cross-section with approximate location of each Phase (1–3). (c) Schematic representation of microstructures associated with Phases 2 and 3 deformation. Rose diagrams summarize the orientations measured in thin section for each phase of deformation and Mohr's circles illustrate the mechanical conditions of formation of the observed microstructures. *Note*. The colored arrows are used to identify the same features in Figures 4–8. Phase 2 deformation is early hydrofracture ($\mu = 0.6$, gray arrows) that is associated with seafloor deformation and alteration. The Rose diagram summarizes the host rock fracture orientations measured in sample WCHU79, and WCHU76. Phase 3 deformation consists of a drop in P_f and an increase in differential stress that resulted in Riedel dilatational shear fractures ($\mu = 0.6$, blue and yellow arrows) that operated coevally with highly mis-oriented, minor slip on chlorite compressional surfaces ($\mu = 0.3$). The Rose diagram summarizes dilatational shear fracture orientations that cut intact basalt lenses and were measured in samples WCHU76, WCHU93, WCHU85, and WCHU92. As deformation progressed and intact basalt was increasingly broken down into fault gouge, Phase 3 deformation was increasingly accommodated on chlorite- and illite-rich gouge ($\mu = 0.3–0.4$) and on non-dilatational Riedel shears ($\mu = 0.3$, white arrows). The Rose diagram summarizes non-dilatational Riedel fracture orientations that were measured in samples WCHU85, WCHU76, WCHU92, and WCHU93. (d) Original photomicrograph of sample WCHU85 and photomicrograph that is annotated with the fracture orientation interpretation. These fractures all developed during progressive Phase 3 deformation and the orientation of σ_1 is assumed to be parallel to the dilatational fractures in yellow.

The deformation represented by the failure mode diagram and Mohr circle plots can be subdivided into two distinct phases (Phases 2 and 3) related to the pattern of deformation described above and illustrated in Figures 10b and 10c. Phase 2 involved brecciation and fracturing at random orientations, indicating hydrofracture conditions where P_f locally exceeded the magnitude of σ_1. It is represented by the gray dot in the tensile field of Mohr's circle (Figure 10c). Phase 2 microstructures may be a relict of seafloor processes that are not necessarily related to subduction; the hydrofractures are randomly oriented and do not indicate formation under differential stresses. Phase 3 involved progressive deformation during fluctuating pore fluid pressure conditions and increasing comminution and gouge formation. Early Phase 3 fractures have a dilatational component and many plot in the "dilatational hydroshear" regime for intact basalt, which is consistent with near-lithostatic pore fluid pressures and differential stresses up to ~17 MPa (Figures 10a and 10c). Once gouge formation became pervasive in the rock, the gouge developed optimally oriented Riedel shear bands in chlorite-rich zones that, with only a rare exception, lack a dilatational component. Therefore, as fault gouge progressively developed, later Phase 3 microstructural orientations suggest a possible decrease in P_f and differential stress. This brackets the differential stress to between ~1.7–17 MPa (Figures 10a and 10c).

We hypothesize that Phase 3 microstructures represent an intermediate stage in the progression of deformation toward an end-member process that is predominantly controlled by the frictional properties of chlorite and illite. Phase 3 deformation likely occurred in a cyclical pattern, with progressively increasing fluid pressures leading to brecciation of basalt fragments within incipient gouge layers, precipitation of more chlorite, and gradual grain size reduction to produce thicker zones of chlorite-rich gouge. The P_f was likely lowered during dilatational fracturing (as fluid is released) such that subsequent failure could occur at lower P_f. As deformation progressed, grain size reduction likely reduced porosity and allowed P_f to build up again. The Mohr circle diagrams indicate that the conditions required for dilatational fracturing of intact basalt are simultaneously sufficient to permit shear slip on misoriented phyllosilicate compressional surfaces such that, as the gouge fabric developed, the compressional surfaces may have accommodated shear slip while P_f remained high. With increasing gouge development, progressive rotation of the compressional fabric into more optimal orientations for shear slip facilitated further weakening and localization into the weak gouge zones, even at lower P_f, culminating in slip on chlorite-dominated (non-dilatational) Riedel shears and eventually along Y-shears oriented parallel to the slip plane. While we do observe one instance of a dilatational fracture cutting cataclasite, these features appear to be rare and there are no dilatational fractures that cut ultracataclastic zones. This could imply that P_f had not yet built up high enough again to cause dilatation along extensional fractures before the basalt was underplated or that P_f conditions remained low past a certain point in the progression of subduction deformation of basalt.

6. Discussion and Implications

6.1. The Role of Pre-Subduction Alteration State in Facilitating Megathrust Weakening

In the Halibut Cove Lagoon rocks, seafloor alteration resulted in partial alteration of the groundmass and the filling of pore spaces with hydrous minerals including chlorite and minor smectite. This alteration likely "set the stage" for weakening of the basalt during subduction in two key ways, including (a) facilitating dehydration of hydrous minerals during subduction burial and associated pore collapse, thus contributing to the observed initial high pore fluid pressures (e.g., Hacker et al., 2003; Kameda et al., 2017, 2011); and (b) facilitating localization of strain into chlorite-rich regions due to its lower friction coefficient relative to intact basalt (e.g., Zhang et al., 2017). These results thus support previous suggestions that the degree of seafloor alteration may be an important consideration not only in the dehydration profile of the megathrust (Kameda et al., 2017; Massonne & Willner, 2008), but also in megathrust shear strength and mechanical behavior (discussed further below; Kameda et al., 2017; Phillips et al., 2019). More generally, the type and degree of seafloor alteration will depend on depth in the oceanic crust, composition of the protolith, composition of circulating fluids, pathways for fluid circulation, and the length of time on the seafloor prior to subduction (e.g., Alt, 1995; Alt et al., 1986; Staudigel, 2003). Some degree of seafloor alteration is widely expected in most subducted basalt, perhaps with the exception of dry slabs (e.g., Juan de Fuca; Canales et al., 2017). Where basalt is pervasively altered (e.g., older oceanic crust and/or vigorous hydrothermal circulation), we hypothesize that it is easier for weaker mineral phases to coalesce and break the basalt down into an anastomosing system of chlorite-rich gouge that surrounds small blocks of unaltered/less altered basalt. Where

basalt is less altered, we might expect less internal deformation/progression toward a chlorite-rich gouge, and strain may instead localize on the margins of unaltered/less-altered basalt blocks or slabs.

6.2. Comparison to Other Basalt-Hosted Natural Faults

In an effort to determine how generally our observations capture the basalt breakdown process, we can compare the features preserved in the Halibut Cove Lagoon fault rocks with other notable examples. Dip-slip normal faults that cut the Faroe Islands Basalt Group during the Paleogene, for example, are not subduction-related but record a remarkably similar microstructural evolution of undeformed host rock basalt toward high strain, pyllosilicate-rich cataclasites surrounded by brecciation (Walker et al., 2013). Another example is found in the Mino Belt in central Japan, which is an accretionary complex with slabs of basalt preserved in an imbricate thrust stack and shear zones that are several meters to tens of meters thick (Niwa, 2006). These shear zones cut through prehnite-pumpellyite-facies pillow lavas and massive basalt and exhibit Riedel shears and phyllosilicate-rich shear bands comparable to those recorded in the Halibut Cove Lagoon rocks (Niwa, 2006). Similarly, the Shimanto accretionary complex near the Nankai Trough of Japan exposes two basalt-hosted subduction-related thrusts and associated basalt-derived cataclasites within the Mugi melange (Kameda et al., 2011, 2017; Phillips et al., 2019; Ujiie et al., 2007). This thrust fault formed at shallower depths and cooler temperatures (at 4–6 km depth and ~150°C–190°C) but have developed layers of cataclasite that are similar to some of the Halibut Cove Lagoon fault rock samples. The basalt-hosted fault rocks in the Mugi melange have been interpreted to represent paleoseismicity that involved the fluidization of cataclasites due to frictional heating that resulted in the transformation of smectite to chlorite during subduction deformation (Kameda et al., 2011; Ujiie et al., 2007) and clasts interpreted to be pseudotachylite within cataclasites (Phillips et al., 2019). This is somewhat different from what we observe in Halibut Cove, where we see no evidence of frictional heating or fluid-supported granular flow, but it is similar in that chlorite concentrations appeared to have increased syn-kinematically during cataclasis.

Based on these examples, we infer that basalt weakens through a similar pattern of deformation mechanisms during shallow crustal deformation (independent of tectonic regime) with a frictional strength that is highly dependent on the presence and quantity of phyllosilicates. This basalt breakdown process is similar to processes observed in continental fault zones where other (nominally dry) igneous rocks such as granite are common. Shallow crustal deformation in granitic rocks exhibit a similar dependence on phyllosilicate content and weakening. Granitic rocks weaken substantially as a result of pre- and syn-kinematic fluid-rock interactions that cause feldspar to be sericitized (Wechsler et al., 2011). This process occurs shallower than 10 km depth and below 350°C, both prior to and in conjunction with cataclasis during fault slip (Wintsch et al., 1995). As the proportion of phyllosilicates gradually increases syn-kinematically during shear, deformation in granite-hosted faults is increasingly dominated by frictional sliding instead of cataclasis (Airaghi et al., 2020; Wibberley, 2005). Similarly to the process recorded in the Halibut Cove Lagoon basalts, the increasing proportion of phyllosilicates results in strain localization and lowering of the frictional strength of the host rock granite.

6.3. Similarities and Differences Compared to Sediment-Dominated Megathrusts

The majority of previously published field and microstructural descriptions of subduction megathrust shear zones focus on those developed primarily in sedimentary decollements or melange belts (e.g., Fagereng & Sibson, 2010; Kimura et al., 2012; Mittempergher et al., 2018; Otsubo et al., 2016; Rowe et al., 2011; Wakabayashi & Rowe, 2015). Comparing our observations from a basalt-hosted megathrust to these examples is important to understanding whether sediment-starved trenches should exhibit distinct differences in stress state along the shallow megathrust relative to sediment-rich environments. We consider two primary aspects that are important in this context, including (a) shear strength along the interface and (b) shear zone widths.

6.3.1. Differences in Shear Strength Along the Interface

The structures in the Halibut Cove Lagoon fault indicate that deformation evolved from initially supra-lithostatic fluid pressures in frictionally strong, altered basalt, to below-lithostatic fluid pressures in frictionally weak, chlorite-dominated fault gouge. The shear stress magnitudes and pore fluid factors estimated in Figure 10c for the chlorite-dominated shear zones (~3–9 MPa, λ = ~0.86–0.96) are consistent with estimates from

modern subduction zones, as constrained by seismic reflection (Bangs et al., 2009; Kitajima & Saffer, 2012; Tobin & Saffer, 2009), inversions of heatflow data (Gao & Wang, 2014), force-balance analyses (Lamb, 2006; Lamb & Davis, 2003; Wang & Suyehiro, 1999), and field studies (Fagereng et al., 2010; Ujiie et al., 2018), all of which indicate integrated shear stresses on the megathrust of less than 20 MPa and elevated fluid pressures. Our observations suggest that this relative weakness on the plate interface in oceanic-crust-dominated environments results from the progressive conversion of altered basalt to chlorite-rich gouge, which exhibits similar frictional properties to phyllosilicates developed in sediment-rich subduction trenches (e.g., illite; Behnsen & Faulkner, 2012; Den Hartog et al., 2012; Fisher & Byrne, 1987) at similar conditions.

Several observations from exhumed exposures of sediment-dominated melanges, however, suggest that extremely high fluid pressures and low effective normal stresses (including switches in the orientation of σ_1) can be transiently maintained to high strains (Cerchiari et al., 2020; Fagereng et al., 2010, 2014; Otsubo et al., 2016; Ujiie et al., 2018). Extremely low effective normal stresses are also implied for shallow interface regions that exhibit tidally modulated slow slip events (e.g., Cochran et al., 2004; Katakami et al., 2017). These data suggest that at least some sediment-dominated interfaces may maintain higher fluid overpressures, perhaps due to faster de-watering and dehydration at shallow conditions than basalts and/or lower permeability in sedimentary sequences due to compaction and mineral alignment (Kerrick & Connolly, 2001; Van Keken et al., 2011). Thus far, similar evidence of maintained fluid overpressures have not been described for exhumed basalt-hosted megathrust fault splays. An additional observation is that many sediment-dominated shear zones exhibit evidence for a balance between cataclasis and thermally-activated processes in quartz, such as pressure solution (which is commonly favored due to the fine grain size of protolith rocks such as shales; Fagereng & Den Hartog, 2017; Fisher et al., 1995; Hashimoto et al., 2006; Mittempergher et al., 2018). Although basalt can host minor quartz during crystallization, and additional quartz can be introduced through alteration and vein precipitation, the quartz concentrations in basalt at shallow conditions are much lower than in sediments. Thus, basaltic protoliths lack significant soluble phases that can promote pressure solution creep, consistent with the lack of evidence for dissolution features or cleavage development in the Halibut Cove Lagoon rocks. Microphysical models of combined frictional-viscous creep suggest a significant strength reduction at depths greater than ~10 km compared to dominant frictional-slip on phyllosilicate layers (Den Hartog et al., 2012; Den Hartog & Spiers, 2013; Fagereng & Den Hartog, 2017).

These comparisons suggest that, although sheared basalt does weaken significantly relative to its undeformed host rock, the deformed product can still potentially host larger shear stresses than some megathrusts developed in sedimentary protoliths where fluid overpressures are maintained over longer timescales and where pressure solution is activated.

6.3.2. Differences in Shear Zone Width

The width of the damage zone and gouge layers within the Halibut Cove Lagoon fault zone is toward the low end of estimates from typical subduction thrust faults (Rowe et al., 2011, 2013; Wakabayashi & Rowe, 2015). Its highly localized expression contrasts sharply with many subduction thrusts developed in sedimentary protoliths, which commonly manifest as several meters-to tens-of-meters-wide melange belts (e.g., Fagereng & Sibson, 2010; Kusky & Bradley, 1999; Meneghini et al., 2009). The high degree of localization in the Halibut Cove Lagoon basalts is likely due to a combination of factors, including the competency contrast between altered host basalt ($\mu = 0.6$) and chlorite-rich gouge ($\mu = 0.3$) in the fault zone (see Section 5.3; Collettini et al., 2011; Fagereng & Sibson, 2010; Goodwin & Tikoff, 2002). Fault zones in sediment-rich environments, by contrast, can exhibit lower competency contrasts between the host rock and a developing fault, e.g., in instances in which the host rock is already rich in phyllosilicates, thus leading to a more typical shear zone width that scales with total displacement (Faulkner et al., 2010; Wibberley et al., 2008). Dissolution-precipitation is favored in sediment-rich fault zones and this can also result in widening of fault zones with flow at lower stresses and strain rates. If we make the simplifying assumption that the less than 1-m-thick Halibut Cove Lagoon fault accommodated the total plate boundary convergence sometime during its history, then for typical plate convergence rates of ~2-10 cm/year, we calculate a minimum strain rate ($\dot{\epsilon} = \delta V / 2\delta x$) of $\dot{\epsilon} = 10^{-8} s^{-1}$. This rate is much faster than typical estimates for steady-state aseismic creep ($\sim 10^{-11} s^{-1}$) where a wider fault zone is assumed. This strain rate estimate may not be applicable if the Halibut Cove Lagoon fault zone does not represent a single megathrust structure but rather a

fault splay within a series of faults that accommodated convergence (though we do not observe field evidence of this). In contrast, meter-to tens-of-meter-wide melange belts for the same convergence rate bounds can accommodate strain rates that are 2–4 orders of magnitude slower, thus are capable of accommodating plate boundary slip at slower steady state rates. Both shear zone types can potentially host faster slip rates on localized slip surfaces within them (e.g., Rowe et al., 2013), which makes these estimates minimum bounds.

6.4. Implications of Basalt-Weakening for Asperity Evolution and Megathrust Seismogenic Slip Behavior

The strain-weakening preserved in the Halibut Cove Lagoon fault basalt has implications for how basalt-dominated bathymetric features on the subduction interface (e.g., seamounts, horst-and-graben topography, and ridge segments) may evolve during progressive subduction. In the case of seamount subduction specifically, numerical and analog models suggest diverse behaviors and stress states as a function of the ratio between the effective strength of the upper plate (accretionary wedge or crystalline basement) and the seamount itself (Baba et al., 2001; Dominguez et al., 2000; Ruh et al., 2016). Keeping all other parameters constant, consideration of strain-weakening in the basaltic crust of the seamount should result in its rapid dismemberment due to localization of strain into discrete and weakened fault zones (Ruh et al., 2016), consistent with observations of thin-skinned duplexing of upper oceanic crustal basaltic fragments in exhumed subduction complexes (e.g., Kimura & Ludden, 1995; Ueda, 2005). The timescale of this process will depend critically, however, on the ability of the upper plate to also weaken with increasing strain (e.g., Ruh et al., 2016). Our results suggest that incorporating a strain-weakening term for the subducting oceanic crust that scales with the degree of seafloor alteration would be a realistic approach to modeling seismic and mechanical behaviors for sediment-poor or topographically rough subduction margins.

The propensity for basalt-dominated asperities occupying the megathrust to generate large earthquakes depends on the velocity-dependence of its frictional properties both in the host rock and the fault gouge zones. Laboratory friction experiments suggest that fresh basalt and gabbro protoliths exhibit velocity-weakening behavior at conditions similar to those observed in the Halibut Cove Lagoon rocks (He et al., 2007; Zhang et al., 2017). Experiments on altered basalt that were run at the slightly lower temperatures also suggest velocity-weakening behavior (Phillips, Belzer, et al., 2020). This implies that unstable slip may nucleate in altered basalt, at least at slightly shallower subduction depths and when the primary alteration product is albite. In contrast, chlorite-dominated gouges consistently show velocity-strengthening friction in laboratory experiments (Ikari et al., 2009; Okamoto et al., 2019). This implies that, as basaltic rocks are subducted to greater depths and become more highly strained, unstable slip nucleation could potentially be suppressed by the transition to chlorite-rich gouge. Thus, taken together, the potential for basalt weakening and the observations that the weakened fault products are velocity strengthening support interpretations that topographic highs on the interface may not necessarily be the nucleation source of large megathrust earthquakes (e.g., Geersen et al., 2015; Wang & Bilek, 2014; Yang et al., 2013). Further observations from basalt-hosted megathrust fault segments, structures in exhumed seamounts, and/or friction experiments on basalt-derived gouge zones would be invaluable in further testing the role of chlorite-rich gouge in subduction zone seismogenesis.

7. Conclusions

Based on field and microstructural observations of an exhumed subduction megathrust fault splay, we show that pre-subduction, seafloor alteration of basalt produced hydrous phases and substantially lowered its frictional strength. Very high P_f was required to initially overcome the strength of intact basalt, which then weakened through a cyclical pattern of brecciation, dilatational shear, and shear slip, culminating in the development of chlorite-rich fault gouge and a decrease from supra-lithostatic to below-lithostatic fluid pressures. Our data suggest that basalt can weaken substantially on the shallow interface, consistent with global observations of low shear stresses in modern subduction zones. However, deformation in basaltic protoliths is more localized, and records higher shear stresses and greater P_f fluctuations than some sediment-hosted megathrusts deformed at similar P-T conditions. Our results suggest that oceanic crustal bathymetric features on the seafloor, particularly where moderately to significantly altered, will dismem-

ber into a chlorite-dominated gouge during shallow subduction; furthermore, the velocity-strengthening frictional properties of chlorite gouge constrained in previously published experiments suggests that these basaltic gouge zones may not be the nucleation source of large megathrust earthquakes.

Data Availability Statement

Supporting Information S1 are available in the ETH Zürich Research Collection at https://doi.org/10.3929/ethz-b-000473661.

Acknowledgments
This research was funded by an ERC Starting Grant to W. M. Behr (S-SIM, Grant No. 947659) and an ETH Zürich Career Seed Grant to Z. Braden (Grant No. 03 19-2). The authors are grateful to J. Allaz for help with the EMP, to Michael Plötze for XRD analyses, to Luiz Morales for help with SEM, and the authors acknowledge support of the Scientific Center for Optical and Electron Microscopy (ScopeM) of the ETH Zurich. The authors would also like to thank L. Hufford, M. Helper, and B. Higman for their support while conducting fieldwork in Alaska. The authors thank Noah Phillips, Don Fisher, and an anonymous Associate Editor for thoughtful comments that improved the manuscript. Open access funding provided by Eidgenossische Technische Hochschule Zurich.

References

Airaghi, L., Bellahsen, N., Dubacq, B., Chew, D., Rosenberg, C., Janots, E., et al. (2020). Pre-orogenic upper crustal softening by lower greenschist facies metamorphic reactions in granites of the central Pyrenees. *Journal of Metamorphic Geology*, *38*(2), 183–204. https://doi.org/10.1111/jmg.12520

Allmendinger, R. W., Cardozo, N., & Fisher, D. M. (2011). *Structural geology algorithms: Vectors and tensors*. Cambridge University Press.

Alt, J. C. (1995). Subseafloor processes in mid-ocean ridge hydrothennal systems. In S. E. Humphris, R. A. Zierenberg, L. S. Mullineaux, & R. E. Thomson (Eds.), *Seafloor hydrothermal systems: Physical, chemical, biological, and geological interactions* (pp. 85–114). American Geophysical Union. https://doi.org/10.1029/GM091p0085

Alt, J. C., Honnorez, J., Laverne, C., & Emmermann, R. (1986). Hydrothermal alteration of a 1 km section through the upper oceanic crust, Deep Sea Drilling Project Hole 504B: Mineralogy, chemistry and evolution of seawater-basalt interactions. *Journal of Geophysical Research: Solid Earth*, *91*(B10), 10309–10335. https://doi.org/10.1029/JB091iB10p10309

Amato, J. M., & Pavlis, T. L. (2010). Detrital zircon ages from the Chugach terrane, southern Alaska, reveal multiple episodes of accretion and erosion in a subduction complex. *Geology*, *38*(5), 459–462. https://doi.org/10.1130/G30719.1

Amato, J. M., Pavlis, T. L., Clift, P. D., Kochelek, E. J., Hecker, J. P., Worthman, C. M., & Day, E. M. (2013). Architecture of the Chugach accretionary complex as revealed by detrital zircon ages and lithologic variations: Evidence for Mesozoic subduction erosion in south-central Alaska. *The Geological Society of America Bulletin*, *125*(11–12), 1891–1911. https://doi.org/10.1130/B30818.1

Baba, T., Hori, T., Hirano, S., Cummins, P. R., Park, J.-O., Kameyama, M., & Kaneda, Y. (2001). Deformation of a seamount subducting beneath an accretionary prism: Constraints from numerical simulation. *Geophysical Research Letters*, *28*(9), 1827–1830.

Bangs, N., Moore, G., Gulick, S., Pangborn, E., Tobin, H., Kuramoto, S., & Taira, A. (2009). Broad, weak regions of the Nankai megathrust and implications for shallow coseismic slip. *Earth and Planetary Science Letters*, *284*(1–2), 44–49.

Barnes, P. M., Wallace, L. M., Saffer, D. M., Bell, R. E., Underwood, M. B., Fagereng, Å., et al. (2020). Slow slip source characterized by lithological and geometric heterogeneity. *Science Advances*, *6*(13), eaay3314.

Beall, A., Fagereng, Å., & Ellis, S. (2019). Fracture and weakening of jammed subduction shear zones, leading to the generation of slow slip events. *Geochemistry, Geophysics, Geosystems*, *20*(11), 4869–4884. https://doi.org/10.1029/2019GC008481

Behnsen, J., & Faulkner, D. R. (2012). The effect of mineralogy and effective normal stress on frictional strength of sheet silicates. *Journal of Structural Geology*, *42*, 49–61. https://doi.org/10.1016/j.jsg.2012.06.015

Behr, W., & Becker, T. W. (2018). Sediment control on subduction plate speeds. *Earth and Planetary Science Letters*, *502*, 166–173.

Behr, W., & Bürgmann, R. (2021). Whats down there? The structures, materials and environment of deep-seated slow slip and tremor. *Philosophical Transactions of the Royal Society A: Mathematical, Physical and Engineering*, *379*.

Behr, W., Kotowski, A. J., & Ashley, K. T. (2018). Dehydration-induced rheological heterogeneity and the deep tremor source in warm subduction zones. *Geology*, *46*(5), 475–478. https://doi.org/10.1130/G40105.1

Bilek, S. L., Schwartz, S. Y., & DeShon, H. R. (2003). Control of seafloor roughness on earthquake rupture behavior. *Geology*, *31*(5), 455–458. https://doi.org/10.1130/0091-7613(2003)031<0455:COSROE>2.0.CO;2

Bourdelle, F., & Cathelineau, M. (2015). Low-temperature chlorite geothermometry: A graphical representation based on a TR2+Si diagram. *European Journal of Mineralogy*, *27*(5), 617–626. https://doi.org/10.1127/ejm/2015/0027-2467

Bourdelle, F., Parra, T., Chopin, C., & Beyssac, O. (2013). A new chlorite geothermometer for diagenetic to low-grade metamorphic conditions. *Contributions to Mineralogy and Petrology*, *165*(4), 723–735. https://doi.org/10.1007/s00410-012-0832-7

Bradley, D. C., & Kusky, T. M. (1990). *Deformation history of the McHugh complex, Seldovia quadrangle, south-central Alaska. Geologic studies in Alaska*. U.S. Geological Survey.

Bradley, D. C., Kusky, T. M., Haeussler, P. J., Karl, S., & Donley, D. T. (1999). *Geologic map of the Seldovia quadrangle, south-central Alaska*. U.S. Geological Survey Open-File Report.

Canales, J. P., Carbotte, S. M., Nedimović, M. R., & Carton, H. (2017). Dry Juan de Fuca slab revealed by quantification of water entering Cascadia subduction zone. *Nature Geoscience*, *10*(11), 864–870. https://doi.org/10.1038/ngeo3050

Cardozo, N., & Allmendinger, R. W. (2013). Spherical projections with OSXStereonet. *Computers & Geosciences*, *51*, 193–205.

Cerchiari, A., Remitti, F., Mittempergher, S., Festa, A., Lugli, F., & Cipriani, A. (2020). Cyclical variations of fluid sources and stress state in a shallow megathrust-zone mélange. *Journal of the Geological Society*, *177*(3), 647–659. https://doi.org/10.1144/jgs2019-072

Clark, S. H. B. (1973). *The McHugh complex of south-central Alaska*. Geological Survey Bulletin.

Clift, P. D., Wares, N. M., Amato, J. M., Pavlis, T. L., Hole, M. J., Worthman, C., & Day, E. (2012). Evolving heavy mineral assemblages reveal changing exhumation and trench tectonics in the Mesozoic Chugach accretionary complex, south-central Alaska. *The Geological Society of America Bulletin*, *124*(5–6), 989–1006. https://doi.org/10.1130/B30594.1

Cloos, M. (1982). Flow melanges: Numerical modeling and geologic constraints on their origin in the Franciscan subduction complex, California. *The Geological Society of America Bulletin*, *93*(4), 330–345.

Cloos, M. (1992). Thrust-type subduction-zone earthquakes and seamount asperities: A physical model for seismic rupture. *Geology*, *20*(7), 601–604.

Cochran, E. S., Vidale, J. E., & Tanaka, S. (2004). Earth tides can trigger shallow thrust fault earthquakes. *Science*, *306*(5699), 1164–1166.

Collettini, C., Niemeijer, A., Viti, C., Smith, S. A., & Marone, C. (2011). Fault structure, frictional properties and mixed-mode fault slip behavior. *Earth and Planetary Science Letters*, *311*(3–4), 316–327.

Cosentino, N. J., Morgan, J., & Jordan, T. (2018). Modeling trench sediment-controlled flow in subduction channels: Implications for the topographic evolution of the central Andean fore arc. *Journal of Geophysical Research: Solid Earth*, *123*(10), 9121–9135.
Cowan, D. S. (1985). Structural styles in Mesozoic and Cenozoic mélanges in the western Cordillera of North America. *The Geological Society of America Bulletin*, *96*(4), 451–462.
Cowan, D. S., & Boss, R. F. (1978). Tectonic framework of the southwestern Kenai Peninsula Alaska. *GSA Bulletin*, *89*(1), 155–158. https://doi.org/10.1130/0016-7606(1978)89<155:TFOTSK>2.0.CO;2
Cox, S. F. (2010). The application of failure mode diagrams for exploring the roles of fluid pressure and stress states in controlling styles of fracture-controlled permeability enhancement in faults and shear zones. *Geofluids*, *10*(1–2), 217–233. https://doi.org/10.1111/j.1468-8123.2010.00281.x
Den Hartog, S. A., Niemeijer, A., & Spiers, C. J. (2012). New constraints on megathrust slip stability under subduction zone p-t conditions. *Earth and Planetary Science Letters*, *353*, 240–252.
Den Hartog, S. A., & Spiers, C. J. (2013). Influence of subduction zone conditions and gouge composition on frictional slip stability of megathrust faults. *Tectonophysics*, *600*, 75–90.
Doebelin, N., & Kleeberg, R. (2015). Profex: A graphical user interface for the Rietveld refinement program BGMN. *Journal of Applied Crystallography*, *48*(5), 1573–1580. https://doi.org/10.1107/S1600576715014685
Dominguez, S., Malavieille, J., & Lallemand, S. E. (2000). Deformation of accretionary wedges in response to seamount subduction: Insights from sandbox experiments. *Tectonics*, *19*(1), 182–196.
Fagereng, Å., & Den Hartog, S. A. M. (2017). Subduction megathrust creep governed by pressure solution and frictional–viscous flow. *Nature Geoscience*, *10*(1), 51–57. https://doi.org/10.1038/ngeo2857
Fagereng, Å., Hillary, G. W. B., & Diener, J. F. A. (2014). Brittle-viscous deformation, slow slip, and tremor. *Geophysical Research Letters*, *41*(12), 4159–4167. https://doi.org/10.1002/2014GL060433
Fagereng, Å., Remitti, F., & Sibson, R. H. (2010). Shear veins observed within anisotropic fabric at high angles to the maximum compressive stress. *Nature Geoscience*, *3*(7), 482–485. https://doi.org/10.1038/ngeo898
Fagereng, Å., & Sibson, R. H. (2010). Mélange rheology and seismic style. *Geology*, *38*(8), 751–754.
Faulkner, D., Jackson, C., Lunn, R., Schlische, R., Shipton, Z., Wibberley, C., & Withjack, M. (2010). A review of recent developments concerning the structure, mechanics and fluid flow properties of fault zones. *Journal of Structural Geology*, *32*(11), 1557–1575.
Fisher, D., Brantley, S. L., Everett, M., & Dzvonik, J. (1995). Cyclic fluid flow through a regionally extensive fracture network within the kodiak accretionary prism. *Journal of Geophysical Research: Solid Earth*, *100*(B7), 12881–12894.
Fisher, D., & Byrne, T. (1987). Structural evolution of underthrusted sediments, Kodiak Islands, Alaska. *Tectonics*, *6*(6), 775–793. https://doi.org/10.1029/TC006i006p00775
Gao, X., & Wang, K. (2014). Strength of stick-slip and creeping subduction megathrusts from heat flow observations. *Science*, *345*(6200), 1038–1041.
Geersen, J., Ranero, C. R., Barckhausen, U., & Reichert, C. (2015). Subducting seamounts control interplate coupling and seismic rupture in the 2014 Iquique earthquake area. *Nature Communications*, *6*(1), 1–6.
Goodwin, L. B., & Tikoff, B. (2002). Competency contrast, kinematics, and the development of foliations and lineations in the crust. *Journal of Structural Geology*, *24*(6–7), 1065–1085.
Hacker, B. R., Abers, G. A., & Peacock, S. M. (2003). Subduction factory 1. Theoretical mineralogy, densities, seismic wave speeds, and H_2O contents. *Journal of Geophysical Research*, *108*(B1).
Hashimoto, Y., Nakaya, T., Ito, M., & Kimura, G. (2006). Tectonolithification of sandstone prior to the onset of seismogenic subduction zone: Evidence from tectonic mélange of the Shimanto Belt, Japan. *Geochemistry, Geophysics, Geosystems*, *7*(6).
He, C., Wang, Z., & Yao, W. (2007). Frictional sliding of gabbro gouge under hydrothermal conditions. *Tectonophysics*, *445*(3), 353–362. https://doi.org/10.1016/j.tecto.2007.09.008
Honnorez, J. (2003). Hydrothermal alteration vs. ocean-floor metamorphism. A comparison between two case histories: The TAG hydrothermal mound (Mid-Atlantic Ridge) vs. DSDP/ODP Hole 504B (Equatorial East Pacific). *Comptes Rendus Geoscience*, *335*(10), 781–824. https://doi.org/10.1016/j.crte.2003.08.009
Humphris, S. E., & Thompson, G. (1978). Hydrothermal alteration of oceanic basalts by seawater. *Geochimica et Cosmochimica Acta*, *42*(1), 107–125. https://doi.org/10.1016/0016-7037(78)90221-1
Husen, S., Kissling, E., & Quintero, R. (2002). Tomographic evidence for a subducted seamount beneath the Gulf of Nicoya, Costa Rica: The cause of the 1990 Mw = 7.0 Gulf of Nicoya earthquake. *Geophysical Research Letters*, *29*(8), 791–794. https://doi.org/10.1029/2001GL014045
Ikari, M. J., & Kopf, A. J. (2011). Cohesive strength of clay-rich sediment. *Geophysical Research Letters*, *38*(16).
Ikari, M. J., Saffer, D. M., & Marone, C. (2009). Frictional and hydrologic properties of clay-rich fault gouge. *Journal of Geophysical Research*, *114*(B5). https://doi.org/10.1029/2008JB006089
Ikari, M. J., Wilckens, F. K., & Saffer, D. M. (2020). Implications of basement rock alteration in the Nankai Trough, Japan for subduction megathrust slip behavior. *Tectonophysics*, *774*, 228275. https://doi.org/10.1016/j.tecto.2019.228275
Insua-Arévalo, J., Tsige, M., Sánchez-Roldán, J., Rodríguez-Escudero, E., & Martínez-Díaz, J. (2021). Influence of the microstructure and roughness of weakness planes on the strength anisotropy of a foliated clay-rich fault gouge. *Engineering Geology*, *289*, 106186.
Kameda, J., Inoue, S., Tanikawa, W., Yamaguchi, A., Hamada, Y., Hashimoto, Y., & Kimura, G. (2017). Alteration and dehydration of subducting oceanic crust within subduction zones: Implications for décollement step-down and plate-boundary seismogenesis. *Earth Planets and Space*, *69*(1), 52. https://doi.org/10.1186/s40623-017-0635-1
Kameda, J., Yamaguchi, A., Saito, S., Sakuma, H., Kawamura, K., & Kimura, G. (2011). A new source of water in seismogenic subduction zones. *Geophysical Research Letters*, *38*(22). https://doi.org/10.1029/2011GL048883
Katakami, S., Yamashita, Y., Yakiwara, H., Shimizu, H., Ito, Y., & Ohta, K. (2017). Tidal response in shallow tectonic tremors. *Geophysical Research Letters*, *44*(19), 9699–9706.
Kerrick, D., & Connolly, J. (2001). Metamorphic devolatilization of subducted oceanic metabasalts: Implications for seismicity, arc magmatism and volatile recycling. *Earth and Planetary Science Letters*, *189*(1–2), 19–29.
Kimura, G., & Ludden, J. (1995). Peeling oceanic crust in subduction zones. *Geology*, *23*(3), 217–220.
Kimura, G., Yamaguchi, A., Hojo, M., Kitamura, Y., Kameda, J., Ujiie, K., et al. (2012). Tectonic mélange as fault rock of subduction plate boundary. *Tectonophysics*, *568–569*, 25–38. https://doi.org/10.1016/j.tecto.2011.08.025
Kirkpatrick, J. D., Fagereng, Å., & Shelly, D. R. (2021). Geological constraints on the mechanisms of slow earthquakes. *Nature Reviews Earth & Environment*, *2*(4), 285–301.

Kitajima, H., & Saffer, D. M. (2012). Elevated pore pressure and anomalously low stress in regions of low frequency earthquakes along the Nankai Trough subduction megathrust. *Geophysical Research Letters*, *39*(23).

Kodaira, S., Takahashi, N., Nakanishi, A., Miura, S., & Kaneda, Y. (2000). Subducted seamount imaged in the rupture zone of the 1946 Nankaido earthquake. *Science*, *289*(5476), 104–106. https://doi.org/10.1126/science.289.5476.104

Kotowski, A. J., & Behr, W. (2019). Length scales and types of heterogeneities along the deep subduction interface: Insights from exhumed rocks on Syros Island, Greece. *Geosphere*, *15*(4), 1038–1065.

Kusky, T. M., & Bradley, D. C. (1999). Kinematic analysis of mélange fabrics: Examples and applications from the McHugh Complex, Kenai Peninsula, Alaska. *Journal of Structural Geology*, *21*(12), 1773–1796. https://doi.org/10.1016/S0191-8141(99)00105-4

Kusky, T. M., Glass, A., & Tucker, R. (2007). Structure, Cr-chemistry, and age of the border ranges ultramafic-mafic complex: A suprasubduction zone ophiolite complex. In K. D. Ridgway, J. M. Trop, J. M. G. Glen, & J. M. O'Neill (Eds.), *Special Paper 431: Tectonic growth of a collisional continental margin: Crustal evolution of southern Alaska* (Vol. 431 pp. 207–225). Geological Society of America. https://doi.org/10.1130/2007.2431(09)

Lallemand, S., Peyret, M., van Rijsingen, E., Arcay, D., & Heuret, A. (2018). Roughness characteristics of oceanic seafloor prior to subduction in relation to the seismogenic potential of subduction zones. *Geochemistry, Geophysics, Geosystems*, *19*(7), 2121–2146.

Lamb, S. (2006). Shear stresses on megathrusts: Implications for mountain building behind subduction zones. *Journal of Geophysical Research*, *111*(B7).

Lamb, S., & Davis, P. (2003). Cenozoic climate change as a possible cause for the rise of the Andes. *Nature*, *425*(6960), 792–797. https://doi.org/10.1038/nature02049

Li, H., Wei, M., Li, D., Liu, Y., Kim, Y., & Zhou, S. (2018). Segmentation of slow slip events in south central Alaska possibly controlled by a subducted oceanic plateau. *Journal of Geophysical Research: Solid Earth*, *123*(1), 418–436. https://doi.org/10.1002/2017JB014911

Li, J., Shillington, D. J., Saffer, D. M., Bécel, A., Nedimović, M. R., Kuehn, H., et al. (2018). Connections between subducted sediment, pore-fluid pressure, and earthquake behavior along the Alaska megathrust. *Geology*, *46*(4), 299–302. https://doi.org/10.1130/G39557.1

Logan, J., Dengo, C., Higgs, N., & Wang, Z. (1992). Fabrics of experimental fault zones: Their development and relationship to mechanical behavior. In R. A. Pielke (Ed.), *International geophysics* (Vol. 51, pp. 33–67). Elsevier.

López-Carmona, A., Kusky, T. M., Santosh, M., & Abati, J. (2011). P-T and structural constraints of lawsonite and epidote blueschists from Liberty Creek and Seldovia: Tectonic implications for early stages of subduction along the southern Alaska convergent margin. *Lithos*, *121*(1–4), 100–116. https://doi.org/10.1016/j.lithos.2010.10.007

Lytwyn, J., Lockhart, S., Casey, J., & Kusky, T. (2000). Geochemistry of near-trench intrusives associated with ridge subduction, Seldovia Quadrangle, southern Alaska. *Journal of Geophysical Research*, *105*(B12), 27957–27978. https://doi.org/10.1029/2000JB900294

Malatesta, C., Gerya, T., Crispini, L., Federico, L., & Capponi, G. (2013). Oblique subduction modelling indicates along-trench tectonic transport of sediments. *Nature Communications*, *4*(1), 1–6.

Massonne, H.-J., & Willner, A. P. (2008). Phase relations and dehydration behaviour of psammopelite and mid-ocean ridge basalt at very-low-grade to low-grade metamorphic conditions. *European Journal of Mineralogy*, *20*(5), 867–879.

Masuda, K., Arai, T., & Takahashi, M. (2019). Effects of frictional properties of quartz and feldspar in the crust on the depth extent of the seismogenic zone. *Progress in Earth and Planetary Science*, *6*(1), 50. https://doi.org/10.1186/s40645-019-0299-5

Meneghini, F., Marroni, M., Moore, J. C., Pandolfi, L., & Rowe, C. D. (2009). The processes of underthrusting and underplating in the geologic record: Structural diversity between the Franciscan Complex (California), the Kodiak Complex (Alaska) and the Internal Ligurian Units (Italy). *Geological Journal*, *27*.

Mittempergher, S., Cerchiari, A., Remitti, F., & Festa, A. (2018). From soft sediment deformation to fluid assisted faulting in the shallow part of a subduction megathrust analogue: The Sestola Vidiciatico Tectonic Unit (Northern Apennines, Italy). *Geological Magazine*, *155*(2), 438–450.

Mochizuki, K., Yamada, T., Shinohara, M., Yamanaka, Y., & Kanazawa, T. (2008). Weak interplate coupling by seamounts and repeating M ~ 7 earthquakes. *Science*, *321*(5893), 1194–1197.

Moore, J. C., & Byrne, T. (1987). Thickening of fault zones: A mechanism of melange formation in accreting sediments. *Geology*, *15*(11), 1040–1043.

Nilsen, T. H., & Zuffa, G. G. (1982). The Chugach Terrane, a Cretaceous trench-fill deposit, southern Alaska. *Geological Society, London, Special Publications*, *10*(1), 213–227. https://doi.org/10.1144/GSL.SP.1982.010.01.14

Niwa, M. (2006). The structure and kinematics of an imbricate stack of oceanic rocks in the Jurassic accretionary complex of Central Japan: An oblique subduction model. *Journal of Structural Geology*, *28*(9), 1670–1684. https://doi.org/10.1016/j.jsg.2006.06.011

Nokleberg, W. J., Plafker, G., Lull, J. S., Wallace, W. K., & Winkler, G. R. (1989). Structural analysis of the Southern Peninsular, Southern Wrangellia, and Northern Chugach Terranes along the trans-Alaska crustal transect, northern Chugach Mountains, Alaska. *Journal of Geophysical Research*, *94*(B4), 4297–4320. https://doi.org/10.1029/JB094iB04p04297

Okamoto, A. S., Verberne, B. A., Niemeijer, A. R., Takahashi, M., Shimizu, I., Ueda, T., & Spiers, C. J. (2019). Frictional properties of simulated chlorite gouge at hydrothermal conditions: Implications for subduction megathrusts. *Journal of Geophysical Research: Solid Earth*, *124*(5), 4545–4565. https://doi.org/10.1029/2018JB017205

Otsubo, M., Miyakawa, A., Kawasaki, R., Sato, K., Yamaguchi, A., & Kimura, G. (2016). Variations in stress and driving pore fluid pressure ratio using vein orientations along megasplay faults: Example from the Nobeoka Thrust, southwest Japan. *Island Arc*, *25*(6), 421–432.

Pavlis, T. L. (1982). Origin and age of the border ranges fault of southern Alaska and its bearing on the Late Mesozoic tectonic evolution of Alaska. *Tectonics*, *1*(4), 343–368. https://doi.org/10.1029/TC001i004p00343

Pavlis, T. L., & Roeske, S. M. (2007). The border ranges fault system, southern Alaska. In K. D. Ridgway, J. M. Trop, J. M. G. Glen & J. M. O'Neill (Eds.), *Special paper 431: Tectonic growth of a collisional continental margin: Crustal evolution of southern Alaska* (Vol. 431, pp. 95–127). Geological Society of America. https://doi.org/10.1130/2007.2431(05)

Perez, R. J. (2005). An empirically derived kinetic model for albitization of detrital plagioclase. *American Journal of Science*, *305*(4), 312–343. https://doi.org/10.2475/ajs.305.4.312

Perras, M. A., & Diederichs, M. S. (2014). A review of the tensile strength of rock: Concepts and testing. *Geotechnical & Geological Engineering*, *2*(32), 525–546. https://doi.org/10.1007/s10706-014-9732-0

Phillips, N. J., Belzer, B., French, M. E., Rowe, C. D., & Ujiie, K. (2020). Frictional strengths of subduction thrust rocks in the region of shallow slow earthquakes. *Journal of Geophysical Research: Solid Earth*, *125*(3), e2019JB018888. https://doi.org/10.1029/2019JB018888

Phillips, N. J., Motohashi, G., Ujiie, K., & Rowe, C. D. (2020). Evidence of localized failure along altered basaltic blocks in tectonic mélange at the updip limit of the seismogenic zone: Implications for the shallow slow earthquake source. *Geochemistry, Geophysics, Geosystems*, *21*(7), e2019GC008839. https://doi.org/10.1029/2019GC008839

Phillips, N. J., Rowe, C. D., & Ujiie, K. (2019). For how long are pseudotachylytes strong? Rapid alteration of basalt-hosted pseudotachylytes from a shallow subduction complex. *Earth and Planetary Science Letters*, *518*, 108–115.

Plafker, G., Nokleberg, W. J., & Lull, J. S. (1989). Bedrock geology and tectonic evolution of the Wrangellia, Peninsular, and Chugach Terranes along the trans-Alaska crustal transect in the Chugach Mountains and Southern Copper River Basin, Alaska. *Journal of Geophysical Research: Solid Earth*, *94*(B4), 4255–4295. https://doi.org/10.1029/JB094iB04p04255

Potel, S. (2007). Very low-grade metamorphic study in the pre-late cretaceous terranes of New Caledonia (Southwest Pacific Ocean). *Island Arc*, *16*(2), 291–305.

Rosenbauer, R. J., Bischoff, J. L., & Zierenberg, R. A. (1988). The laboratory albitization of mid-ocean ridge basalt. *The Journal of Geology*, *96*(2), 237–244.

Rowe, C. D., Meneghini, F., & Moore, J. C. (2009). Fluid-rich damage zone of an ancient out-of-sequence thrust, Kodiak Islands, Alaska. *Tectonics*, *28*(1).

Rowe, C. D., Meneghini, F., & Moore, J. C. (2011). Textural record of the seismic cycle: Strain-rate variation in an ancient subduction thrust. *Geological Society, London, Special Publications*, *359*(1), 77–95. https://doi.org/10.1144/SP359.5

Rowe, C. D., Moore, J. C., Remitti, F., & Scientists, I. E. T. (2013). The thickness of subduction plate boundary faults from the seafloor into the seismogenic zone. *Geology*, *41*(9), 991–994.

Ruh, J. B., Sallarès, V., Ranero, C. R., & Gerya, T. (2016). Crustal deformation dynamics and stress evolution during seamount subduction: High-resolution 3-D numerical modeling. *Journal of Geophysical Research: Solid Earth*, *121*(9).

Saffer, D. M., & Bekins, B. A. (2006). An evaluation of factors influencing pore pressure in accretionary complexes: Implications for taper angle and wedge mechanics. *Journal of Geophysical Research: Solid Earth*, *111*(B4). https://doi.org/10.1029/2005JB003990

Saffer, D. M., & Marone, C. (2003). Comparison of smectite- and illite-rich gouge frictional properties: Application to the updip limit of the seismogenic zone along subduction megathrusts. *Earth and Planetary Science Letters*, *215*(1), 219–235. https://doi.org/10.1016/S0012-821X(03)00424-2

Saffer, D. M., & Wallace, L. M. (2015). The frictional, hydrologic, metamorphic and thermal habitat of shallow slow earthquakes. *Nature Geoscience*, *8*(8), 594–600. https://doi.org/10.1038/ngeo2490

Scholz, C. H., & Small, C. (1997). The effect of seamount subduction on seismic coupling. *Geology*, *25*(6), 487–490. https://doi.org/10.1130/0091-7613(1997)025<0487:TEOSSO>2.3.CO;2

Sobolev, S. V., & Babeyko, A. Y. (2005). What drives orogeny in the Andes? *Geology*, *33*(8), 617–620. https://doi.org/10.1130/G21557AR.1

Staudigel, H. (2003). Hydrothermal alteration processes in the oceanic crust. In H. D. Holland, & K. K. Turekian (Eds.), *Treatise on geochemistry* (pp. 511–535). Pergamon. https://doi.org/10.1016/B0-08-043751-6/03032-2

Tobin, H. J., & Saffer, D. M. (2009). Elevated fluid pressure and extreme mechanical weakness of a plate boundary thrust, Nankai Trough subduction zone. *Geology*, *37*(8), 679–682.

Tréhu, A. M., Blakely, R. J., & Williams, M. C. (2012). Subducted seamounts and recent earthquakes beneath the central Cascadia forearc. *Geology*, *40*(2), 103–106. https://doi.org/10.1130/G32460.1

Ueda, H. (2005). Accretion and exhumation structures formed by deeply subducted seamounts in the Kamuikotan high-pressure/temperature zone, Hokkaido, Japan. *Tectonics*, *24*(2).

Ujiie, K., Saishu, H., Fagereng, Å., Nishiyama, N., Otsubo, M., Masuyama, H., & Kagi, H. (2018). An explanation of episodic tremor and slow slip constrained by crack-seal veins and viscous shear in subduction mélange. *Geophysical Research Letters*, *45*(11), 5371–5379. https://doi.org/10.1029/2018GL078374

Ujiie, K., Yamaguchi, A., Kimura, G., & Toh, S. (2007). Fluidization of granular material in a subduction thrust at seismogenic depths. *Earth and Planetary Science Letters*, *259*(3), 307–318. https://doi.org/10.1016/j.epsl.2007.04.049

Van Keken, P. E., Hacker, B. R., Syracuse, E. M., & Abers, G. A. (2011). Subduction factory: 4. Depth-dependent flux of H_2O from subducting slabs worldwide. *Journal of Geophysical Research: Solid Earth*, *116*(B1).

Van Rijsingen, E., Lallemand, S., Peyret, M., Arcay, D., Heuret, A., Funiciello, F., & Corbi, F. (2018). How subduction interface roughness influences the occurrence of large interplate earthquakes. *Geochemistry, Geophysics, Geosystems*, *19*(8), 2342–2370.

Von Huene, R., Ranero, C. R., & Vannucchi, P. (2004). Generic model of subduction erosion. *Geology*, *32*(10), 913–916.

Vrolijk, P., Myers, G., & Moore, J. C. (1988). Warm fluid migration along tectonic melanges in the Kodiak Accretionary Complex, Alaska. *Journal of Geophysical Research*, *93*(B9), 10313–10324. https://doi.org/10.1029/JB093iB09p10313

Wakabayashi, J., & Rowe, C. D. (2015). Whither the megathrust? Localization of large-scale subduction slip along the contact of a mélange. *International Geology Review*, *57*(5–8), 854–870.

Walker, R. J., Holdsworth, R. E., Imber, J., Faulkner, D. R., & Armitage, P. J. (2013). Fault zone architecture and fluid flow in interlayered basaltic volcaniclastic-crystalline sequences. *Journal of Structural Geology*, *51*, 92–104. https://doi.org/10.1016/j.jsg.2013.03.004

Wang, K., & Bilek, S. L. (2014). Invited review paper: Fault creep caused by subduction of rough seafloor relief. *Tectonophysics*, *610*, 1–24.

Wang, K., & Suyehiro, K. (1999). How does plate coupling affect crustal stresses in northeast and southwest Japan? *Geophysical Research Letters*, *26*(15), 2307–2310.

Watts, A. B., Koppers, A. A. P., & Robinson, D. P. (2010). Seamount subduction and earthquakes. *Oceanography*, *23*(1), 166–173.

Wechsler, N., Allen, E. E., Rockwell, T. K., Girty, G., Chester, J. S., & Ben-Zion, Y. (2011). Characterization of pulverized granitoids in a shallow core along the San Andreas Fault, Littlerock, CA. *Geophysical Journal International*, *186*(2), 401–417. https://doi.org/10.1111/j.1365-246X.2011.05059.x

Wibberley, C. A. J. (2005). Initiation of basement thrust detachments by fault-zone reaction weakening. *Geological Society, London, Special Publications*, *245*(1), 347–372. https://doi.org/10.1144/GSL.SP.2005.245.01.17

Wibberley, C. A. J., Yielding, G., & Di Toro, G. (2008). Recent advances in the understanding of fault zone internal structure: A review. *Geological Society, London, Special Publications*, *299*(1), 5–33.

Wiewióra, A., & Weiss, Z. (1990). Crystallochemical classifications of phyllosilicates based on the unified system of projection of chemical composition: II. The chlorite group. *Clay Minerals*, *25*(1), 83–92. https://doi.org/10.1180/claymin.1990.025.1.09

Wintsch, R. P., Christoffersen, R., & Kronenberg, A. K. (1995). Fluid-rock reaction weakening of fault zones. *Journal of Geophysical Research: Solid Earth*, *100*(B7), 13021–13032. https://doi.org/10.1029/94JB02622

Yang, H., Liu, Y., & Lin, J. (2013). Geometrical effects of a subducted seamount on stopping megathrust ruptures. *Geophysical Research Letters*, *40*(10), 2011–2016.

Zhang, G., Germaine, J. T., Martin, R. T., & Whittle, A. J. (2003). A simple sample-mounting method for random power X-ray diffraction. *Clays and Clay Minerals*, *51*(2), 218–225. https://doi.org/10.1346/CCMN.2003.0510212

Zhang, L., He, C., Liu, Y., & Lin, J. (2017). Frictional properties of the South China Sea oceanic basalt and implications for strength of the Manila subduction seismogenic zone. *Marine Geology*, *394*, 16–29. https://doi.org/10.1016/j.margeo.2017.05.006